

# Mechanisms of Coulomb dissociation processes

Zoltán Seres ‡

Wigner Research Centre for Physics, Hungarian Academy of Sciences, Hungary

E-mail: [seres.zoltan@wigner.mta.hu](mailto:seres.zoltan@wigner.mta.hu)

**Abstract.** The Coulomb dissociation is studied of the  $^8\text{Li}$  nuclei on Pb target at energies 40.3 and 69.5 MeV/nucleon, in the experiment NSCL #03038. The  $^6,7\text{Li}$ ,  $^4,6\text{He}$ , and  $^2\text{H}$  fragments were identified. The resonance decay and the direct breakup reactions were observed. The data give experimental evidence that the Coulomb dissociation is a two step process. The projectile in the approaching phase is braked down and the valence neutron gets forced oscillation. The increasing Coulomb force holds the projectile and brings through the excited states up to the closest approach point. There released, the projectile is trapped into a primary, highly excited state in the continuum. The lifetime of the primary excited state depends on the multipolarity of the deformed projectile. At intermediate energy the collision is a sudden reaction, the valence neutron may stay — during the impact — in the forward or backward hemisphere of the projectile nucleus, and the orbit of the valence neutron gets prolate or oblate, dipole or multipole deformation and the nucleus gets single-particle or collective excitation. The primary excited states, developing will decay prompt or delayed into the same reaction channel, resulting in the two decay mechanisms.

## 1. Introduction

In large impact parameter collisions, when the closest approach distance is larger than the sum of the two radii, the Coulomb interaction may induce nuclear reactions. In the experiment NSCL #03038 the  $\text{Pb}(^8\text{Li}, ^7\text{Li}+n)\text{Pb}$  Coulomb breakup reaction was investigated because of its astrophysical interest [1, 2] and to study the mechanism of the reaction. The intermediate and high energy light ions in the strong electric field of a high  $Z$  target nucleus may suffer Coulomb dissociation. The Coulomb breakup gives sharp peaks above the particle threshold with large transition strength of long lived, low energy unbound resonance states, the soft dipole resonances [3, 4]. However, in other experiments there were observed fragments faster than the beam [5, 6]. Supposedly those decayed in the Coulomb field of the target nucleus and after the decay the fragments were post-breakup accelerated with  $Z/A$  changed. It requests that the lifetime of the excited state must be many orders of magnitude less than the lifetime calculated by the uncertainty principle from the width of the known unbound resonance levels. This

‡ For the MoNA collaboration: ELTE (Budapest), NSCL(East Lansing), Atomki (Debrecen), Rykkyo (Tokyo), and Wigner Research Centre for Physics (Budapest), in experiment NSCL #03038.

paper analyzes the data of the above experiment in order to investigate the reaction mechanisms of the Coulomb dissociation.

The post-acceleration was not found in every experiment. In the Coulomb dissociation of 41 MeV/nucleon  $^{11}\text{Be}$  there could not be verified the post-acceleration in the longitudinal velocity of the fragments [7, 8]. But K. Riisager *et al.* [9] found that the neutron velocity was shifted down, emitted from the decelerated projectile in the Coulomb dissociation of 29 MeV/nucleon  $^{11}\text{Li}$  on gold target. D. Sackett *et al.* [10, 5] found that the velocity difference of the fragments and neutrons was definitely larger than zero ( $\Delta v = v_9 - v_{2n} = 0.0090 \pm 0.0003 c$ ) in the Coulomb breakup of 28 MeV/nucleon  $^{11}\text{Li}$  on Pb target. They explained it with post-breakup acceleration of the fragment.

A lot of theoretic effort was invested to study the post-acceleration of the fragments. G. Baur *et al.* shew that the longitudinal post-breakup acceleration of the fragment can be estimated in a classical model, however, it was absent in quantal model based on Glauber theory in sudden approximation [11]. The higher order electromagnetic interaction may play decisive role in the post-breakup acceleration [12]. G. F. Bertsch and C. A. Bertulani [13] calculated the longitudinal momentum shift of the fragment of the  $^{11}\text{Li} \rightarrow ^9\text{Li} + 2n$  Coulomb dissociation at 28 MeV/nucleon energy. They solved the time-dependent Schrödinger equation in one dimension, and got post-acceleration of the fragment in the order of magnitude of the measured value. They compared the quantum prediction with the classical model of instantaneous decay where the neutron is fixed to the projectile up to the closest approach point and there decays. The quantum and the instantaneous models give similar post-acceleration values in the 20–50 fm impact parameter range. Sagawa *et al.* [6] studied the multipole excitation of the valence nuclei. They concluded that the extremely large transition strength, the sharp peak above the particle threshold is non collective, single-particle excitation. T. Kido *et al.* [14] solved numerically the time dependent Schrödinger equation in the external Coulomb field of the target nucleus. They took a single neutron and the core, expanding the external field into multipoles. From the time evolution the post-breakup acceleration, the relative longitudinal momentum shift was under estimated by a factor of 2.

Some statements in the upper papers serve relevance for the conclusions derived from the data of the present experiment as follows. At intermediate and high energy the Coulomb disintegration is a *sudden process*, for the beam velocity is much larger than the intrinsic motion of the valence neutron [7, 11, 13]. The dissociation on heavy target, at large impact parameter is *dominated by the Coulomb excitation*, the contribution of the Coulomb-nuclear interference and nuclear interaction is small at impact parameters in the order of 20 fm [7, 15]. The projectile is *excited direct to the continuum*. The excited states concentrate in a *narrow region around the giant resonances* [15]. The resonances *decay mostly by particle*, or are attenuated by  $\gamma$ -ray emission (at a few tenth of MeV/nucleon energy the  $\gamma$ -ray multiplicity is about 10 [16]). The *time delay* of the particle emission can play an important role in the Coulomb dissociation process [13]. The *instantaneous decay model* gives realistic result on the contrary the raw classical

approximation [13].

The experimental setup is described in Sec. 2. The acceptance of the fragment detector and the magnetic field cut small phase space cells separating several fragments of different  $Z$  and  $A$ , momenta and scattering angle, *i.e.* several reaction channels. The fragment identification is described in Sec. 3. At 40 MeV/nucleon the  ${}^7\text{Li}$ ,  ${}^6\text{Li}$ ,  ${}^6\text{He}$ , and  ${}^4\text{He}$ , at 70 MeV/nucleon the  ${}^7\text{Li}$ ,  ${}^6\text{Li}$ ,  ${}^4\text{He}$ , and  ${}^2\text{H}$  fragments can be separated. The yield of the reaction channels is discussed in Sec. 4. The two reaction mechanisms are presented and verified in Sec. 5. The decays of the long-lived unbound resonance states are discussed in Sec. 6. Low-lying resonance states are identified of the  ${}^8\text{Li}$ ,  ${}^7\text{Li}$ , and  ${}^6\text{Li}$  nuclei. The direct breakup reaction is analyzed in Sec. 7. The neutron and fragment velocity spectra are compared and their correlation is investigated. It was found that the neutron velocity of the resonance and the direct breakup reaction has identical structure, the reaction products are from the same final transitions. The correlation of the velocities verifies the identification of the fragment charge.

An explanation of the observed phenomena is proposed in Sec. 8. It is supposed that the Coulomb dissociation is a two step breakup process. The projectile in the approaching phase is slowed down by the Coulomb field and the valence neutron gets forced oscillation. The increasing long range external force pushes over the projectile through the excited states and strongly deforms the orbit of the valence neutron. The projectile survives the collision and surpassing the closest approach, released is trapped into a highly excited state in the continuum. The lifetime of the primary excited state depends on the multipolarity of the oscillation. The state of short lifetime decays prompt in the Coulomb field of the target nucleus, while the long living state decays delayed, the excited projectile escapes from the Coulomb field and decays in-flight. The reaction channels are fed from up downwards by the rest of the beam. This is called *leakage model of the decay*. The intermediate and high energy Coulomb dissociation is a sudden process, the beam velocity is larger than the velocity of the orbital motion. During the impact the valence neutron stays with equal probability in the forward and backward hemisphere of the projectile. That is the *localized valence neutron model*. In the forward hemisphere the deformation is prolate with dominantly dipole oscillation and single-particle excitation, in the backward hemisphere oblate deformation, multipole oscillation and collective excitation. The dipole excited nucleus decays prompt, the multipole delayed. The secondary decay, the final fragments inherit the lifetime of the primary decay. So the same fragments can be prompt or delayed decay products, the resonance and the direct breakup processes coexist.

It must be mentioned in advance that the paper presents the experimental data and in the analysis two simplifications were applied. The events are taken to Coulomb breakup and the nuclear interaction and interferences are neglected (those are less than 6% [17]). The fragment tracks are approximated by circles in homogeneous magnetic field. From the observed phenomena qualitative statements are taken and an explanation is proposed on semi-classical base. These simplifications do not destroy the main message of the experiment, *i.e.* the inverse population of the reaction channels and

that the direct breakup events are really resonance decay events, the projectiles from the low lying unbound resonance state decay prompt in the Coulomb field of the target nucleus.

## 2. Experimental setup

The experiment was performed at the Coupled Cyclotron Facility of the NSCL. The  $^8\text{Li}$  ions were produced by 120 MeV/nucleon  $^{18}\text{O}$  beam bombarding a  $2850\text{ mg/cm}^2$  thick  $^9\text{Be}$  primary target and separated by the A1900 isotope separator. The  $^8\text{Li}$  beam energy was 40.3 and 69.5 MeV/nucleon (named 40 and 70 MeV/nucleon below) with a dispersion of FWHM=1.8 MeV/nucleon. The reaction target was  $56.7\text{ mg/cm}^2$  Pb.

The coincidences of the reaction products were measured by the MoNA-FPD (Modular Neutron Array and Focal Plane Detector) coincidence spectrometer (fig. 1) [17]. The MoNA neutron detector consists of 144 pieces of  $200 \times 10 \times 10\text{ cm}^3$  plastic scintillator bars arranged in 9 vertical walls of 16 bars [18]. The MoNA was placed in the beam direction at zero degree at  $D = 832\text{ cm}$  from the target.

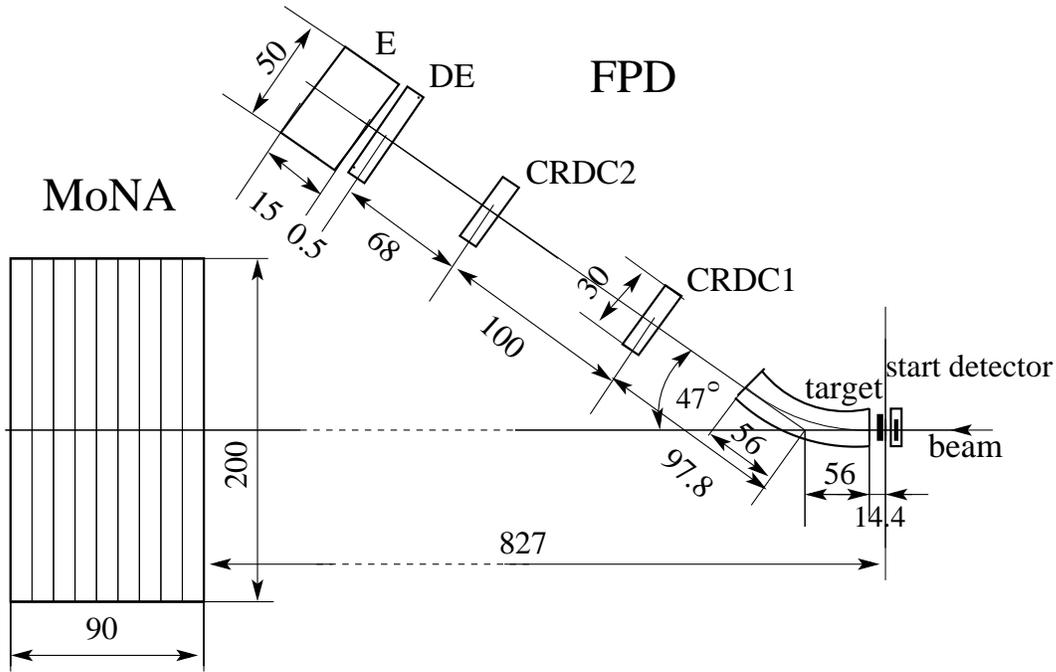


Figure 1: MoNA-FPD coincidence spectrometer (distances in cm).

The fragments were analyzed by a narrow sweeper magnet [19] followed by the FPD. The FPD is a telescope of two Cathode Readout Drift Chamber (CRDC) track detectors [20], and a DE, E scintillator pair. The CRDC-s have  $30 \times 30\text{ cm}^2$  area, 128 horizontal pads. The vertical position was calculated from the drift time measured on the anode of the CRDC-s. The distance of the two CRDC-s was 100 cm at an angle  $47^\circ$  from the beam direction in the laboratory system. The size of the DE and E plastic scintillators was  $50 \times 50 \times 0.5$  and  $50 \times 50 \times 15\text{ cm}^3$ , respectively.

The magnetic field was set to separate the high velocity fragments rising from the Coulomb dissociation with  $v_F > 0.8 v_{proj}$  for fragments A/Z between 2 and 3.

### 3. Data processing

The parameters used in the analysis are: the neutron hit position and the time of flight (TOF) in the MoNA, and the fragment hit position and charge in the CRDC-s, the charge value of the 4 PMT-s of the DE and E scintillation detectors, and the fragment TOF in the FPD. The fragment–neutron coincidence events are accepted if the CRDC and scintillator telescopes had valid track, and the MoNA bars had valid TOF values at both sides.

The FPD and the MoNA detectors started the event taking individually. A common MoNA QDC gate started the charge integration, while the TDC-s were started individually by the PMT-s and stopped by the delayed signal of the start detector. The fragment TOF was measured in indirect mode. The TDC-s were started by the FPGA clock pulse gated by one of the PMT-s of the DE detector firing and stopped by the delayed individual PMT-s of the DE, E, and the start detector. The events were read out and stored if the MoNA–FPD coincidence condition was fulfilled. The coincidence was checked by a coincidence gate started by one the DE detector firing. If no coincidence happened, a fast clear process (FCL) was started. The MoNA FCL was not working, therefore the coincident neutron firing was sitting on several MoNA single data. Because of this error the neutrons of the good coincidence events have no charge value, the MoNA QDC gate was already closed when the coincidence events arrived, and the accidental MoNA TDC-s went to overflow. The average MoNA bar multiplicity was 12 (fig. 2(a)), of the selected neutrons 1–3 (b) (see later).

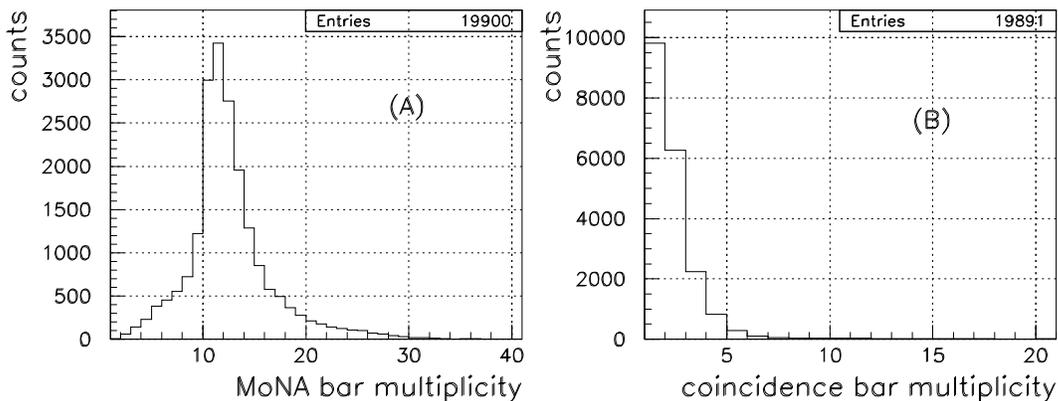


Figure 2: MoNA bar multiplicity (a) all bars, (b) valid coincidence bars, at 40 MeV/nucleon.

The start scintillator was a 26 mg/cm<sup>2</sup> plastic scintillator in front of the target, giving a  $\Delta E = 2.3$  MeV energy loss. The fragments were accepted if both the CRDC

and scintillator telescopes have valid values:

$$F = (CRDC1 \& CRDC2) \& (DE \& E). \quad (1)$$

For the true neutron hit selection there was introduced the class parameter of the MoNA hits (fig. 3):

$$CL = 1 \cdot QL + 2 \cdot TL + 4 \cdot QR + 8 \cdot TR. \quad (2)$$

Q-s and T-s are the charge and time flags [0,1] of the left and right PMT-s of the MoNA bars. The valid neutron firings are the neutrons of class  $CL = 10$  and  $15$  (TT and QQTT events). The coincidence events have 1-3 bars firing (fig. 2(b)). Finally every event was coincidence event, the proper neutron was selected with high probability only it had no valid charge value. The share of the accidental neutron coincidences is estimated, it is a few percent.

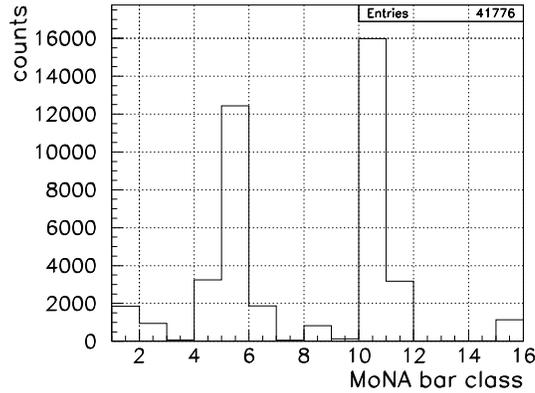


Figure 3: MoNA bar class spectrum of the 40 MeV/nucleon coincidence events.

### 3.1. Neutron detection

The MoNA hit position was determined from the bar sequence number — in the beam and vertical direction — and horizontally from the time of flight difference of the light along the bar:  $x = (t_R - t_L)/v_{light}$ , where  $t$  is the TOF measured by the PMT-s at the right and left end of the bar and  $v_{light}$  the light velocity in the scintillator. The  $t_n$  TOF of the neutrons is the mean value of the right and left measured TOF values:  $t_n = (t_R + t_L)/2$ .

The first MoNA hit of the coincidence events was accepted for the neutron hit. That is the closest to the target, the direct neutron hit. The MoNA hit map in coincidence with the  ${}^6\text{Li}$  fragments is shown in fig. 4. The hits are concentrated around the beam direction. The scatter plot has fluctuations. The horizontal structure refers to discrete groups of the  ${}^6\text{Li}+n$  channel. In fig. 5(a) there is shown the spectrum of the bar frequency of the MoNA. There is a 16-th periodicity with decreasing amplitude. The particles are flying in the beam direction, they emerge from the target. The horizontal distributions are symmetric peaks to the beam direction.

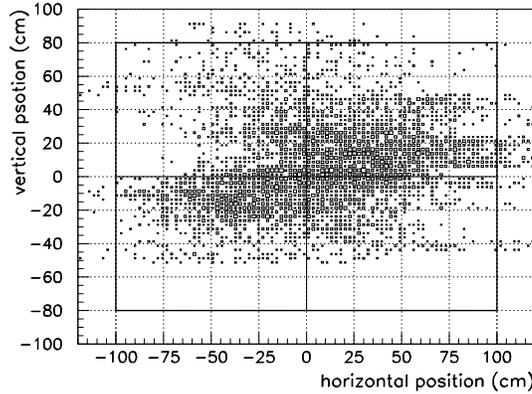


Figure 4: MoNA hit map of  ${}^6\text{Li}+n$  coincidence events at 70 MeV/nucleon.

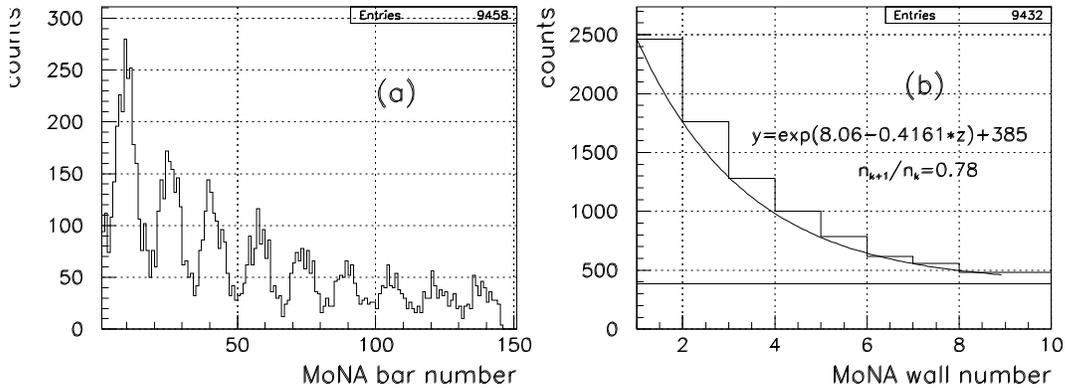


Figure 5: (a) MoNA bar frequency of 70 MeV/nucleon coincidence events, (b) attenuation of the neutrons from the target.

The particles are neutrons. The area of the peaks decreases exponentially on a constant (cosmic-rays) background (fig. 5(b)). The detection probability of one bar is 0.6.

The time calibration of the MoNA TDC channels of the individual PMT-s was performed in two steps. The channels were normalized together by cosmic-rays, and the absolute values were calibrated by target  $\gamma$ -rays. The error of the TOF value was  $\text{FWHM}=0.3$  ns by 75 ns beam TOF (70 MeV/nucleon). The error of the horizontal position calculated from the time of flight of the light in the scintillator was  $\pm 6$  cm at 827 cm target–MoNA distance.

### 3.2. Fragment identification

The published paper [2] focused to the cross section of the 70 MeV/nucleon  ${}^7\text{Li}+n$  breakup process and did not analyzed the other fragments and the 40 MeV/nucleon data. The investigation of the reaction mechanisms in the present analysis is based on the whole spectrum of the fragments detected.

The CRDC parameters are the sequence number of the firing pads, the charge measured on the pads and the drift time of the anode signal. The horizontal position

of the hit was the charge weighted mean of the pads. The standard deviation of the horizontal position was 0.4 mm and the angular acceptance in dispersive  $7^\circ$ . The vertical position was calculated from the drift time measured at the anode. The scintillator telescope measured the  $DE$  and  $E$  charge produced by the fragments and the TOF values.

The fragment identification is performed in two steps. First the fragments are classified into groups and then the  $Z$  and  $A$  are assigned to the groups based on the energy and the correlation of the fragment and neutron velocities. The grouping of the fragments was performed only by the direct measured parameters: CRDC hits, scintillator  $DE$ ,  $E$  charges and the  $DE$  TDC (TOF) values. The asymptotic tracks are shown in fig. 6 of the  ${}^6\text{Li}$  fragments — between the CRDC-s — at 70 MeV/nucleon. Two kinds of particle tracks can be observed. There are parallel, close to perpendicular and crossing tracks: the resonance and direct breakup events.

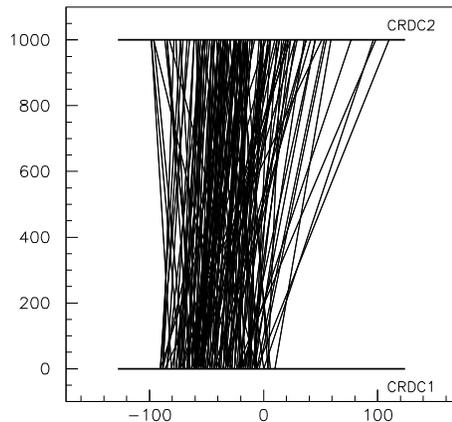


Figure 6: Asymptotic tracks in the CRDC telescope of  ${}^6\text{Li}$  fragments at 40 MeV/nucleon.

From the CRDC telescope coordinates one can calculate the slope of the asymptotic tracks in the CRDC-s frame as  $SL = (w_2 - w_1)/d$ , where  $w$ -s are the hit coordinates in mm ( $w = \pm 150$  mm) and  $d = 1000$  mm the distance of the CRDC-s (fig. 7). The error of the track slope is 0.1%. In the plot of the  ${}^6\text{Li}$  track slope at 70 MeV/nucleon, there is a narrow peak of the resonance decay events and a broad one of the direct breakup events. The spectrum is fitted by two Gaussian functions (S) and (D) (the parameters are: amplitude, position, and standard deviation of the peaks). The ratio of the two components is 50–50%.

The path of flight of the fragments in the magnet was approximated fitting a circular orbit across the target point and the outgoing track in a constant magnetic field. Therefore the fragment path is a rough approximation, but at small scale it proved to be admissible (the error of the path of flight  $\Delta L/L < 1\%$ ). This simplified analysis is satisfactory for relative and qualitative statements. The reaction channel can be identified by the fragment data, while the neutron data can give information about the decay process.

The fragment energy spectra of the scintillator telescope are shown in the contour

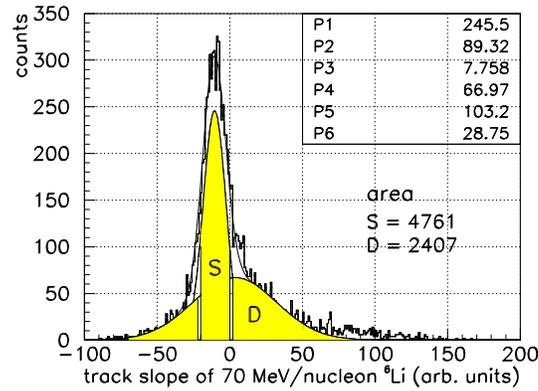


Figure 7: Slope of the asymptotic tracks of  ${}^6\text{Li}$  fragments at 70 MeV/nucleon energy fitted by two Gaussian functions.

plots  $dE$  vs  $E$  in fig. 8 at 40 and 70 MeV/nucleon energies. The charge values of the DE and E scintillators are calibrated to the  ${}^4\text{He}$  group calculated with the program DONNA. For the other ions the  $dE_\alpha$  and  $E_\alpha$  values are approximations neglecting the difference of the light output for different ions and the non linearity of the photomultipliers. Several isotope groups can be observed at both energies, but the plots are not appropriate for fragment separation.

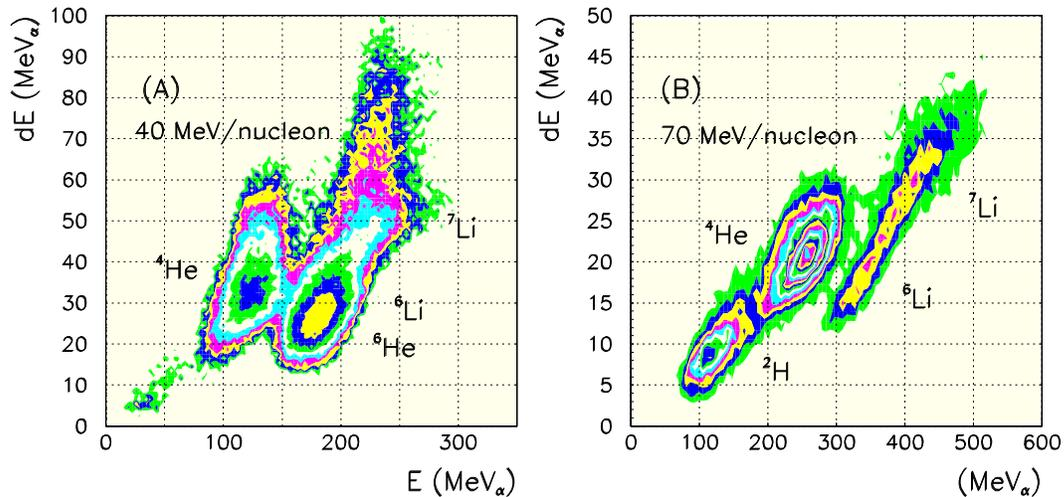


Figure 8: Fragment  $dE$  vs  $E$  contour plots (A) at 40 and (B) at 70 MeV/nucleon. The axes are calibrated to the  ${}^4\text{He}$ .

The kinematic behavior of the fragments can be studied in the velocity map of the fragment TOF vs PoF fragment path of flight. As the fragment path is a rough approximation, instead of the velocity the TOF vs SL contour plot is used for classification of the events (fig. 9), which are direct measured parameters.

At 40 MeV/nucleon (A) three and at 70 MeV/nucleon (B) two groups are well separated. For the separation the groups one can construct concentric circles which fit to the curvature of the groups. The events can be characterized by the radius of a circle

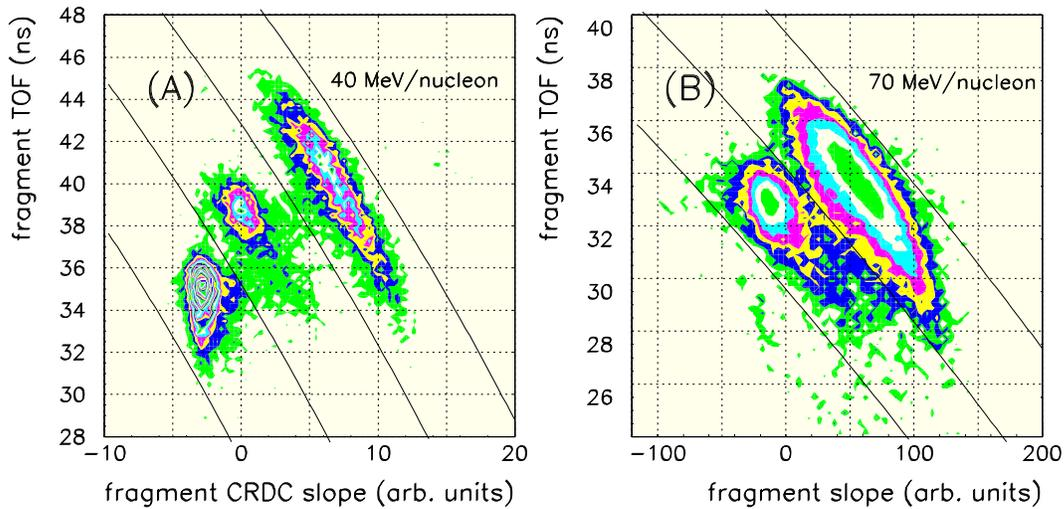


Figure 9: Fragment TOF *vs* slope of the asymptotic tracks (A) at 40 and (B) at 70 MeV/nucleon. The lines are examples of iso-separation lines.

crossing the point of the event and concentric with the cutting ones. The separation radius parameter  $R_s$  is an arbitrary pseudo parameter: the distance of the point from circle crossing the origin of the plot.

$$R_s = \sqrt{(x - x_0)^2 + (y - y_0)^2} - \sqrt{x_0^2 + y_0^2}, \quad (3)$$

where  $x$  and  $y$  are the  $SL$  slope and  $TOF$  coordinates and  $x_0$  and  $y_0$  are the coordinates of the center of the concentric circles. The separation radius is ordered to the event. It is an empirical parameter for separation the fragments one by one according to their kinematic parameters: momentum, scattering angle, and charge. The groups are well separated. They can be cut with a definite efficiency. Some iso-separation lines are plotted to show the quality of the separation.

The sum energy of the fragment  $E = E_\alpha + dE_\alpha$  is an appropriate parameter for the fragment identification. The  $E$  *vs*  $R_s$  plots give consummate separation of the fragments (fig. 10). The separation of the groups at higher energy is better. In the plots four groups can be separated at 40 and 70 MeV/nucleon. The boxes are the limits of the interval tests. There are a triple group and a fourth one. The fourth groups are different corresponding to the two magnetic field settings. The mass number can be read out from the plots, from the energy of the ions. The groups are at  $A = 4, 6, 7$  times 40, and  $A = 2, 4, 6, 7$  times 70 MeV energy. Supposing that the events are neutron-fragment coincidences, a charge can be assigned to the groups. The identification is verified by the velocity correlations of the fragment and the neutron (see Sect. 7.3). At 40 MeV/nucleon  ${}^7\text{Li}$ ,  ${}^6\text{Li}$ ,  ${}^6\text{He}$ ,  ${}^4\text{He}$  fragments, at 70 MeV/nucleon  ${}^7\text{Li}$ ,  ${}^6\text{Li}$ ,  ${}^4\text{He}$ , and  ${}^2\text{H}$  can be identified. The suggested decay scheme of the  ${}^8\text{Li}$  is shown in fig. 11 [21, 22]. The possible observed transitions are signed with the energy and velocity values. The latter are in brackets in cm/ns unit.

This fragment identification method can be useful during the data taking, on-line,

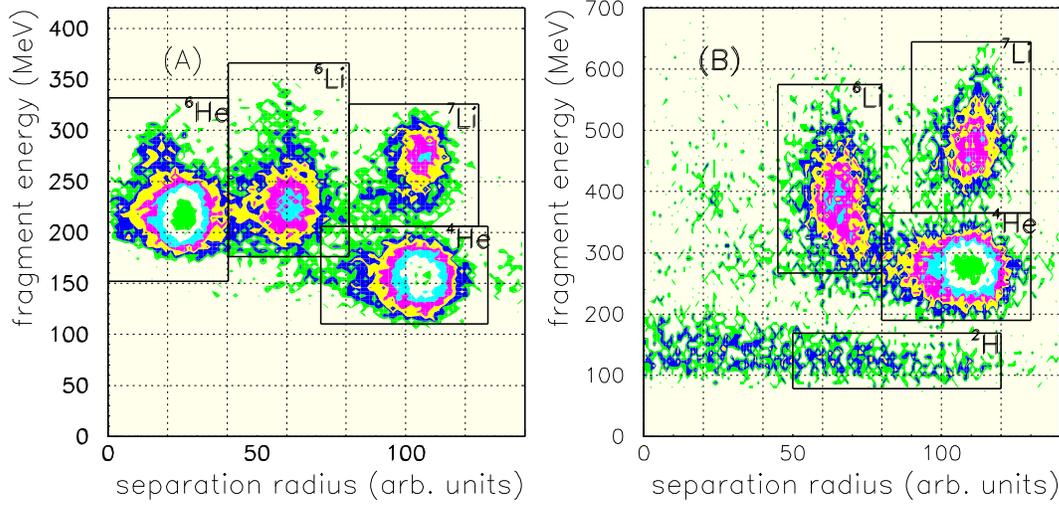


Figure 10: Fragment energy *vs* separation radius at (A) 40 and (B) 70 MeV/nucleon. The boxes are the separating intervals.

for it does not need special calibration and time consuming calculations.

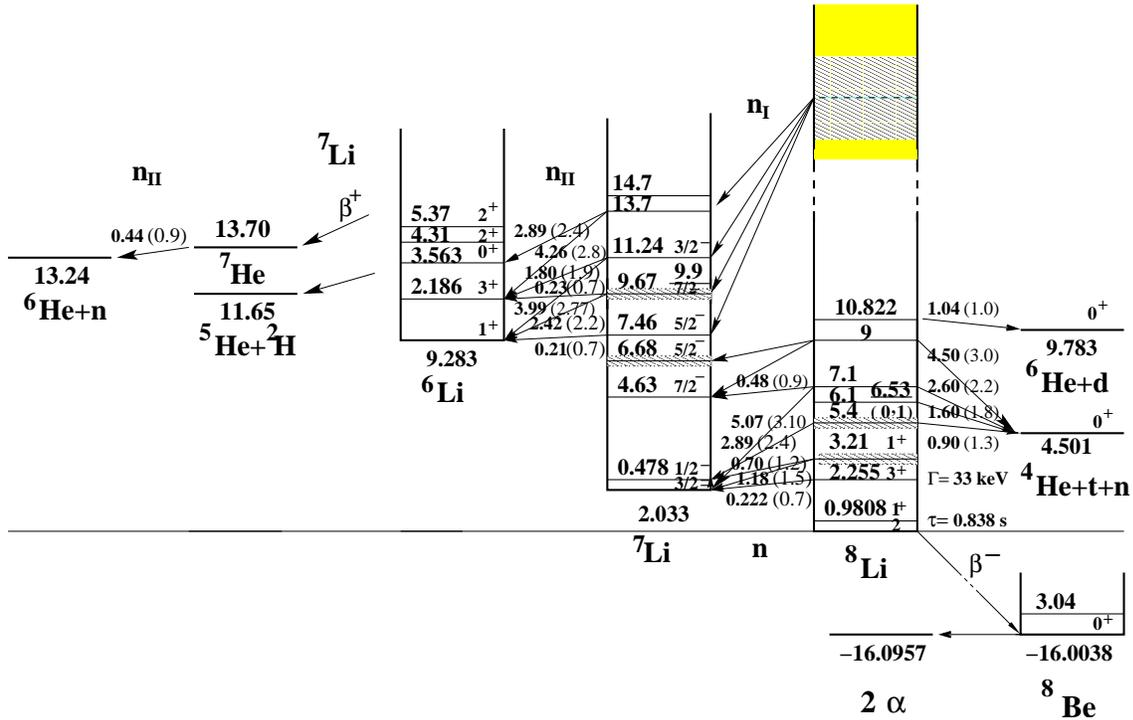


Figure 11:  $^8\text{Li}$  decay scheme [21]. The neutron decay energy and velocity (in brackets) are in MeV and cm/ns.

#### 4. Inverse population ratio

The threshold of the reaction channels is rather high. The  ${}^4\text{He}+t+n$  channel opens above 4.5, the  ${}^6\text{Li}$  channel above 9.28, the  ${}^2\text{H}$  channel above 11.65, the  ${}^6\text{He}+n$  channel 13.7 MeV. The events of the  ${}^6\text{He}+d$  channel are accidental neutron coincidence events. The  ${}^4\text{He}+t+n$  is a three particle final state, the spectra are broader. The  ${}^6\text{Li}+2n$ , the  ${}^5\text{He}+{}^2\text{H}+n$  are two-step, and the  ${}^6\text{He}+\beta+2n$  reaction is three-step process. The relative yields of the fragments are listed in table 1. read from the plots fig. 10. The share of the  ${}^7\text{Li}+n$  channel is 14 and 16% at 40 and 70 MeV/nucleon. The errors are the statistical errors.

At 40 MeV/nucleon the dominating reaction channel is the  ${}^6\text{He}$  with 36%, next is the  ${}^4\text{He}$  27%, and the  ${}^6\text{Li}+2n$  channel with 23%. It has to be noticed that the  ${}^6\text{He}+d$  channel is overrepresented because of the accidental single-MoNA-fragment coincidences. The share of the  ${}^6\text{Li}$  and the  ${}^2\text{H}$  is reduced because of the two-step decay, and the small geometric efficiency of the MoNA for the high energy neutrons (about 20%). The real order of the branching is probably  ${}^6\text{He}$ ,  ${}^2\text{H}$ ,  ${}^6\text{Li}$ ,  ${}^4\text{He}$ , and  ${}^7\text{Li}$ . From the intensity ratios at both energies the conclusion is plausible that the  ${}^8\text{Li}$  is excited high into the giant resonance region and decaying feeds the different reaction channels. The larger the energy of the secondary excited state, the larger the decay probability through that channel. That is called *inverse population ratio*. The reaction channels are fed from up to downwards by the rest of the beam particles.

Table 1: Relative yield of fragments.

beam energy MeV/nucleon	fragment	threshold MeV	counts	partition %
40	${}^6\text{Li}$	9.28	9105	$23\pm 0.24$
40	${}^7\text{Li}$	2.03	5537	$14 \pm 0.19$
40	${}^4\text{He}$	4.50	11000	$27 \pm 0.25$
40	${}^6\text{He}+d$	9.78	13604	$34 \pm 0.29$
40	${}^6\text{He}+n$	13.7	950	$2 \pm 0.06$
70	${}^6\text{Li}$	9.28	9458	$24\pm 0.25$
70	${}^7\text{Li}$	2.03	6896	$16\pm 0.19$
70	${}^4\text{He}$	4.50	21114	$52 \pm 0.36$
70	${}^2\text{H}$	11.65	3076	$8 \pm 0.14$

#### 5. Reaction mechanisms

For studying the reaction mechanism of the Coulomb dissociation processes the best example is the  ${}^6\text{Li}+2n$  channel because of the best statistics. The reaction is a sequential

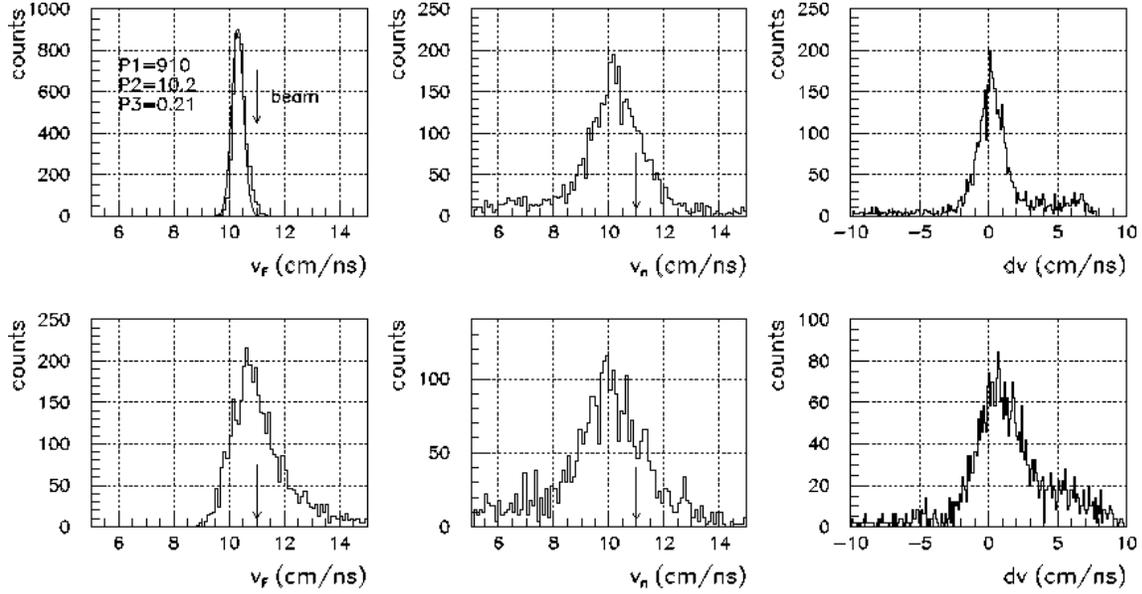


Figure 12: Fragment and neutron velocities of  ${}^6\text{Li}+n_{II}$  coincidences of 70 MeV/nucleon  ${}^6\text{Li}+2n$  reaction channel. Resonance (upper) and direct breakup events (lower row). The left column is the fragment, middle the neutron velocities and the right one  $dv = v_F - v_n$ . The fit is a Gaussian distribution.

two-step decay:  ${}^8\text{Li}^* \rightarrow {}^7\text{Li}^* + n_{II}$  and  ${}^7\text{Li}^* \rightarrow {}^6\text{Li} + n_{II}$ . The neutrons  $n_{II}$  in the 2<sup>nd</sup> step of the dissociation are low energy ones.

Figure 7 shows the slope spectrum of the asymptotic tracks of the  ${}^6\text{Li}$  in the CRDC frame, at 70 MeV/nucleon. It is fitted by two Gaussian functions. The narrow peak is the in-flight decaying long-lived resonance decay (group S) and the tail the direct breakup process (group D). The two reaction mechanisms can be separated confidently.

To verify the two reaction mechanisms in fig. 12 there are plotted the  $v_F$  fragment and  $v_n$  neutron velocities, and the  $dv = v_F - v_n$  velocity differences in cm/ns of the 70 MeV/nucleon  ${}^7\text{Li}^* \rightarrow {}^6\text{Li} + n_{II}$  reaction. The upper row shows the resonance (group S) and the lower row the direct breakup events (group D) gated by the track slope parameter (fig. 7). The beam velocity is 11.0 cm/ns. Left column is the fragment, the middle the neutron velocities and the right one the  $dv$  velocity difference.

The fragment velocity peak of the escaped and in-flight decayed resonance group is narrow. The contribution of the D component in the resonance section of the velocity spectra is less than 5%. The standard deviation is  $\sigma = 0.21$  cm/ns, which corresponds to 23 keV. The velocity shift is  $v_s = -0.8$  cm/ns. The velocity difference  $dv$  is a narrow peak around zero. The neutron velocity has a peak with sequential decay structure, symmetric to the fragment peak. It will be discussed in Sec. 6.1. The velocity spectra of the direct breakup events are broader because the position of the decay in the Coulomb field is not definite. The post-breakup acceleration of the fragments produces a large velocity tail above the beam velocity. The neutron velocity spectrum has similar structure as the resonance group but shifted down (about 0.1 cm/ns) and broader. This supports

the conjecture that the direct breakup is also a resonance-like, but prompt sequential decay process of a source braked down inside the Coulomb field.

Similar plots can be produced from the other reaction channels at 40 and 70 MeV/nucleon.

## 6. Delayed, resonance decay

The neutron velocity spectrum of the resonance decay events (group S) is a sequential neutron decay spectrum. The fully re-accelerated excited projectile decays in-flight emitting a discrete energy neutron (fig. 12). The reaction products are kinematic focused. The velocity spectrum of discrete resonance decay particles emitted into  $4\pi$  solid angle is a trapezoid function. If the transverse momentum is larger than a certain value the particles will miss the detectors, fall out of their solid angle. The middle of the trapezoid spectrum will be cut out and the spectrum consists from a symmetric peak pair of the forward and backward emitted neutrons. The particles are detected in a cone of  $\Phi_0$  limiting angle. The limiting angle for the decay momentum  $q$  in the laboratory frame is:

$$\phi_0 = \arcsin\left(\frac{X}{\sqrt{D^2 + X^2}} \cdot \frac{p}{q}\right) \pm \arctan\left(\frac{X}{D}\right), \quad (4)$$

where  $D$  is the target–detector distance,  $X$  is the half of the detector size,  $p$  is the momentum of the beam velocity particle in the moment of the decay, taking into account the deceleration and the excitation velocity loss. The cutting results in a gap at the middle of the spectrum. However, the velocity and angular dispersion of the beam expands the velocity region, that will be cut but at the same time it will fill the gap and can form a pileup peak in the middle overlapping region. The limiting velocity according to equ. (4) is  $v_c = 0.1193v_0$  cm/ns.

### 6.1. ${}^6\text{Li}+2n$ channel

The velocity spectrum of the  ${}^6\text{Li}$  group S has a resonance character (fig. 12). The narrow peak and the correlation of the  ${}^6\text{Li}$ –neutron velocities (Sect. 7.3.1) verify that the fragments are from the decay of a resonance state  ${}^7\text{Li}^* \rightarrow {}^6\text{Li}+n_{II}$ . The threshold energy of the reaction channel is 9.28 MeV. One has to suppose that the  ${}^8\text{Li}^*$  fell into a long living resonance state high in the continuum, re-accelerated escaped from the Coulomb field of the target nucleus and emitting a neutron fell into a highly excited resonance state of the  ${}^7\text{Li}^*$  (above 7.46 MeV), which decayed in-flight into  ${}^6\text{Li}+n_{II}$ . The decay energy can be estimated from the  $\Delta E_n$  neutron energy increment corrected for the recoil on an  $A_F$  mass fragment  $E_D = \Delta E_n(1 + 1/A_F)$ .

The neutron velocity spectrum of the 70 MeV/nucleon  ${}^6\text{Li}+n_{II}$  resonance events is shown in fig. 13. It consists of a single (S1) and two double peaks (S2 and S3) symmetric to the single one. The peaks are fitted by Gaussian distributions. The symmetry axis is shifted down by  $v_s = -0.8$  cm/ns related to the beam velocity. The resonance decay particles have a definite velocity deficit.

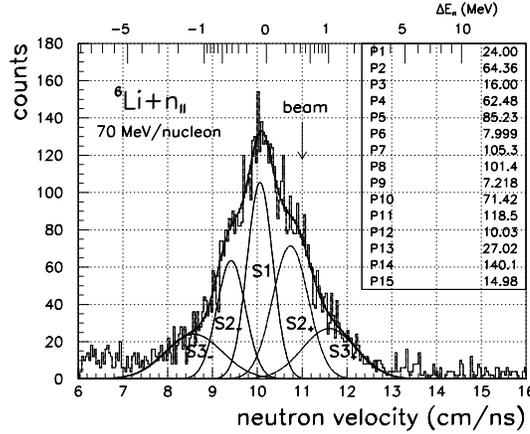


Figure 13: Neutron velocity spectrum of  ${}^6\text{Li}+n_{II}$  resonance decay events at 70 MeV/nucleon cut by track slope gate S. The S1–S3 are Gaussian function fits. The fits are in 0.04 cm/ns units.

The distances of the S2 and S3 peaks from the symmetry axis are  $\Delta v_n = (v_+ - v_-)/2 = \pm 0.61$  and 1.5 cm/ns. These velocities are compatible with the decay scheme of the  ${}^7\text{Li}$  [21] (fig.11). The decay velocity of the totally separated peaks (S3) are underestimated. The spectrum of the group is cut, and the decay velocity is the extreme forward–backward velocity value, however, the fit gives the center of the sections. The standard deviation of the peak has to be added. With  $\sigma = 0.62$  cm/ns the neutron velocity shift is  $\Delta v_{nS3} = \pm 2.12$  cm/ns. The S2 groups are in the cone of the solid angle of the MoNA, but the beam dispersion expands the dynamics of the neutrons and the wings of the distributions are cut outside and give a pileup peak in the middle. The central peak S1 with  $v_D = 0 \pm 0.35$  cm/ns has no equivalent transition. It must be the pileup peak of the S2 transition. The recoil corrected decay velocities are  $v_D = (1 + 1/A_F) \cdot \Delta v_n = 0.71$  and 2.47 cm/ns. The 9.67 MeV state of the  ${}^7\text{Li}$  decays to the first excited and the ground state of the  ${}^6\text{Li}$  with  $v_D = 0.7$  and 2.2 cm/ns neutron emission.

With Monte Carlo simulation the 30% overshoot can be produced by 20% overlap of the forward–backward sections. The plots in fig. 14(A) and (B) simulate the neutron velocity spectra measured in coincidence with the  ${}^6\text{Li}$  fragments at 70 MeV/nucleon energy. The 0.21 MeV transition is simulated with  $v_D = 0.7$  cm/ns decay velocity. The limiting momentum  $q$  is 47 MeV/c ( $E_D = 1.2$  MeV) at 70 MeV/nucleon. Therefore the decay velocity is inside the acceptance of the MoNA and FPD, however, the effective velocity range is extended by the velocity and the angular dispersion of the beam. The parameters of the simulation are the velocities corresponding to the dispersion of the beam energy (1.8 MeV/nucleon), the angular dispersion (0.06 rad), the velocity resolution (0.04 cm/ns) and the limiting momentum (eq. 4). The limiting neutron velocity is fitted to reproduce the spectra at both energies:  $v_c = 0.76$  and 0.81 cm/ns at 40 and 70 MeV/nucleon. The neutrons of the higher decay energy events give separated

peaks. Figure 14(B) shows the simulation of the 2.42 MeV transition. Please notice that the peaks are not Gaussian functions and the decay velocity is at the edge of the peaks.

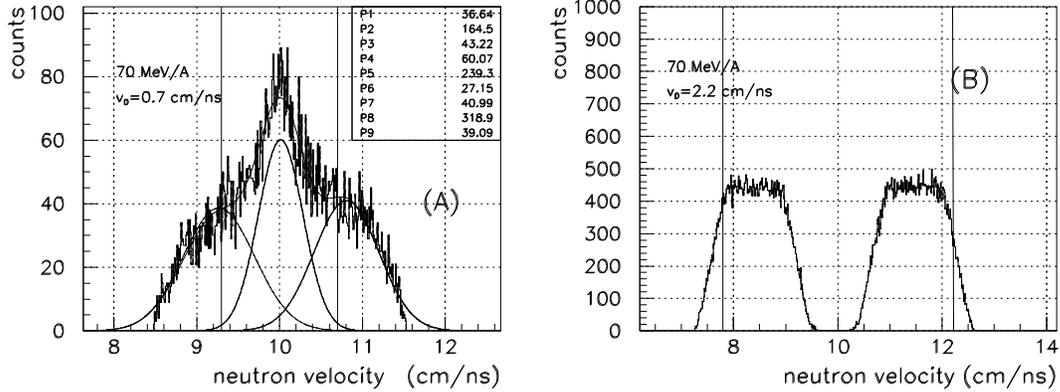


Figure 14: Monte Carlo simulation of the neutron velocity spectra of the 0.21 MeV ( $v_D = 0.7$  cm/ns) (A) and the 2.42 MeV ( $v_D = 2.2$  cm/ns) transitions (B) at 70 MeV/nucleon. The vertical lines show the  $v_D$  decay velocity.

The other fragments have also resonance decay events. Those can be selected by the track slope parameter, or the fragment–neutron velocity difference, however, the separation of the two mechanisms is less clear.

## 7. Prompt, direct breakup

In the direct breakup process the dissociation happens in the Coulomb field of the target nucleus. The  $(A,Z)$  projectile is braked down in the strong repulsing field, emits a particle and the residual  $(A-a,Z-z)$  fragment will be accelerated. The energy stored in the Coulomb potential accelerates the fragment. The specific energy loss and gain of a charged particle is proportional to the path taken with different  $Z/A$ . The relative specific energy increment of the fragment in the Coulomb field is  $\varepsilon = (Z_F/A_F - Z/A)/(Z/A)$ . The relative velocity increment of the fragment, the post-breakup acceleration, is the square root of the specific energy excess  $\Delta v_F/\Delta v_n = -\sqrt{\varepsilon}$ . Here it is assumed that the velocity decrease of the neutron is equal with the velocity loss of the source, *i.e.* of the projectile in the moment of the decay. The post-breakup acceleration is suitable for the fragment identification of a fragment group with known mass number.

### 7.1. Neutron velocity of prompt breakup events

The structure of the neutron velocity spectra can be studied by their cross-correlation function with a searching form function [23]. In fig. 15 there are shown the neutron velocity spectra and their cross-correlation with a Gaussian searching function of the

${}^6\text{Li}+n$  resonance and prompt decay events at 40 and 70 MeV/nucleon energy. The cross-correlation code calculates the difference between the channel content and the mean value in a sliding surrounding window weighted by the form function of the searched peaks. The statistical error, the square root of the mean is added to the mean value. (The cross-correlation method is used in the automatic spectrum analysis codes.) The standard deviation of the form function was  $\sigma = 0.15$  and  $0.25$  cm/ns at 40 (A) and 70 MeV/nucleon (B), and the searching window was  $\pm 2\sigma$  wide. The cross-correlation function is:

$$C(i) = \sum_{j=-k}^k G(j) \cdot \left( F(i+j) - (\overline{F(i)} + \sqrt{\overline{F(i)}}) \right) \quad (5)$$

$$j = -k, \dots, 0, \dots, k$$

$$G(j) = \frac{1}{\sqrt{2\pi}\sigma} \exp\left(-\frac{j^2}{2\sigma^2}\right) \quad (6)$$

$$\overline{F(i)} = \frac{1}{2k+1} \sum_{j=-k}^k F(i+j), \quad (7)$$

where  $C$  is the cross-correlation function of the  $F$  velocity spectrum with a normalized Gaussian searching function  $G$ .

The peak structure of the cross-correlation functions verifies that the neutrons are emitted from excited states with discrete excitation energy. The cross-correlation functions of the delayed resonance (a) and the prompt, direct decay spectra (b) have identical structure at both energies, although they originated from different decay processes. This refers to common origin. The peaks in the cross-correlation plots are labeled with numbers. The spectrum of the 70 MeV/nucleon events (D) has a strong central peak (No. 1.) and some symmetric satellite peak pairs. At 40 MeV/nucleon (B) the central peak is split because of the less kinetic focusing (cut forwards/backwards). The beam velocities are 8.55 and 10.99 cm/ns. The symmetry axes, (peaks No. 1), are shifted down by  $v_s = -0.8$  cm/ns relative to the beam velocity. At 40 MeV/nucleon the resonance and direct breakup spectra are rather similar because of the separation of the two decay mechanisms is not sharp.

The velocity deficit corresponds to the kinetic energy spent to the excitation of a primary high energy state  ${}^8\text{Li}^*$  in the continuum  $v_s = v_x$ . At 70 MeV/nucleon the impact parameter was  $b = 20$  fm [17]. Neglecting the perpendicular displacement of the track the Coulomb potential of a Li ion at 20 fm from the Pb target nucleus is 18 MeV. The  ${}^8\text{Li}$  is a dripline nucleus, the  ${}^7\text{Li}$  core can be taken as structure less particle which binds the valence neutron weakly. The  $v_s = -0.8$  cm/ns velocity shift of the escaped projectile, the resonance decay, corresponds to 24.9 MeV/c momentum transfer to the continuum particles, in agreement with the plot shown in ref. [13]. In case of single particle excitation the deformation and the excitation energy is concentrated to the valence neutron which takes 199 MeV/c momentum or 21 MeV excitation energy.

The down shifted symmetry axes is the velocity of the fully re-accelerated, binding energy corrected projectile  $v_0 = v_{beam} - v_x$ . It was found, that  $v_0$  is common for the

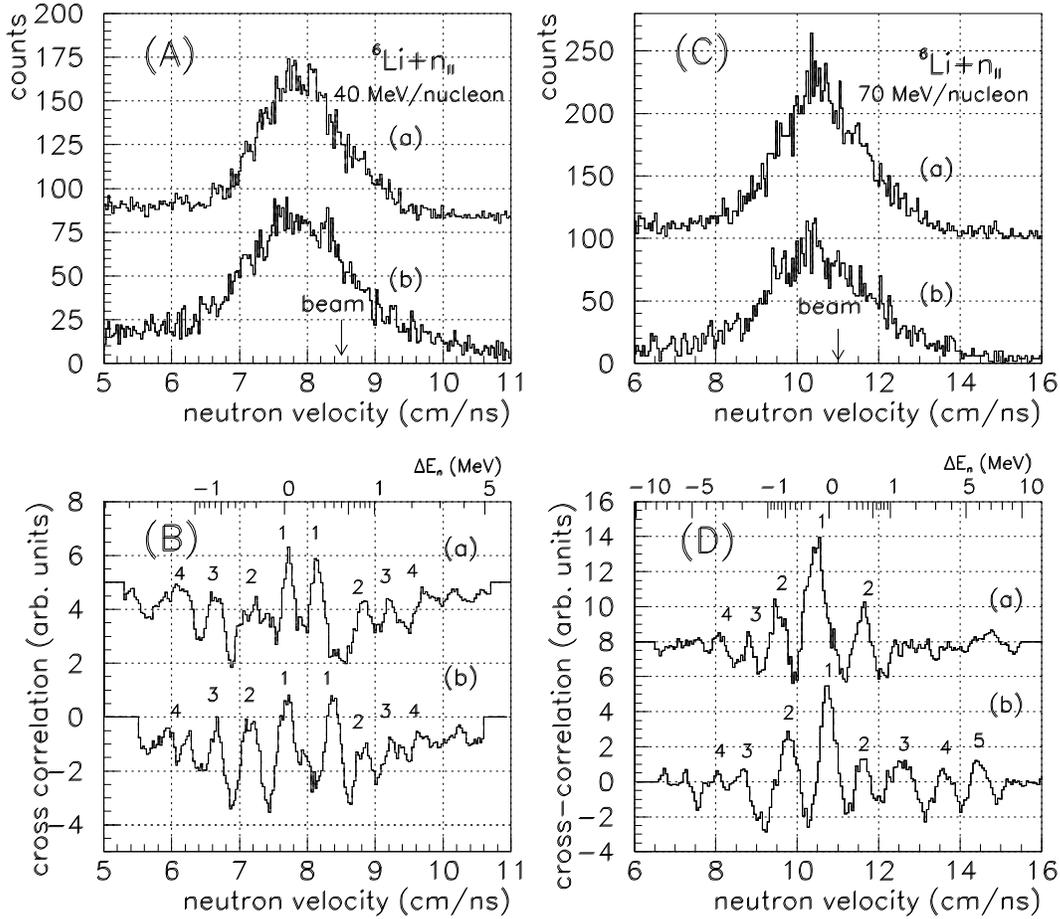


Figure 15: Neutron velocity spectra of the  ${}^6\text{Li}+n_{II}$  channel (A) at 40 and (C) 70 MeV/nucleon energies. (B) and (D) are their cross-correlation functions by a Gaussian searching function with  $\sigma = 0.15$  and  $0.25$  cm/ns standard deviation, respectively. (a) is the resonance and (b) the direct breakup components.

${}^6\text{Li}$ ,  ${}^7\text{Li}$ , and  ${}^4\text{He}$  reaction channels  $v_0 = 7.8$  and  $10.2$  cm/ns at 40 and 70 MeV/nucleon, respectively. The peaks can be co-ordinated to each other in the prompt and resonance cross-correlation spectra. The position of the peaks in the cross-correlation spectrum depends on the environment. The large peak shifts the side ones. The error can be in the order of  $\pm 0.2$  cm/ns. The measured, recoil charged decay velocity ( $v'_D = A/(A+1) \cdot v_D$ ) can be read out from fig. 15. The average of the peak pairs:  $v'_D = (v_+ - v_-)/2$ , where  $v_{\pm}$  are the position of the forward, backward peaks. At 70 MeV/nucleon the peak No. 1 is a single peak in the center. The recoil corrected decay velocities of the peaks are:  $v_{D2} = 0.8$ ,  $v_{D3} = 1.8$ , and  $v_{D4} = 2.6$  cm/ns. These peaks can be identified with the  ${}^7\text{Li}^* \rightarrow {}^6\text{Li}+n$  decay. The transitions from the three levels above the threshold energy of the  ${}^7\text{Li}$  7.46, 9.67, and 11.24 MeV to the ground and two excited states of the  ${}^6\text{Li}$  correspond to the measured peaks with 0.7, 1.9, 2.2, or 2.4 cm/ns decay velocities. The peak No. 1. has no corresponding transition. It must be the pileup peak of the peaks No. 2 at  $v_0$ , because of the dispersion of the beam velocity. At 40 MeV/nucleon the

peak No. 3. (1.4 cm/ns) cannot be identified in the decay scheme, but the  $v_{D2} = 0.8$ ,  $v_{D4} = 1.8 \pm 0.2$  cm/ns transitions can be verified.

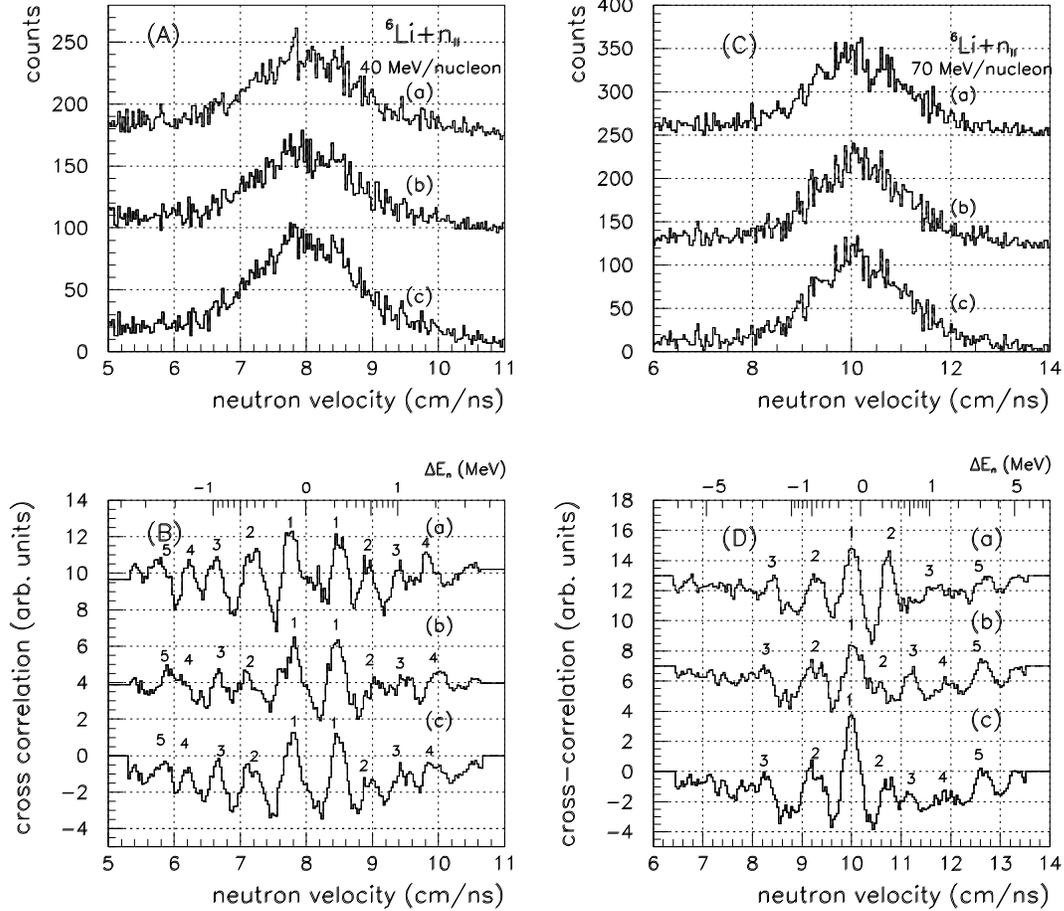


Figure 16: Neutron velocity spectra of the  ${}^6\text{Li}$  direct breakup events at 40 (A) and 70 MeV/nucleon energy (C). (B) and (D) are their cross-correlation functions by a Gaussian searching function with  $\sigma = 0.15$  and  $0.25$  cm/ns standard deviation, respectively. The curves (a), (b), and (c) are the two halves of the events, and the full statistics.

Regarding the simplified analysis and the poor statistics the question occurs whether are the peaks true or accidental ones? In order to verify that the structure of the neutron velocity spectrum is true, it corresponds to the decay, to the Coulomb breakup process, the data of the direct breakup events are cut into two halves and their cross-correlation functions are compared in fig. 16 at both energies. Most of the peaks can be identified in both halves and at both energies. The comparison of the two halves of the events verifies that the peaks are real peaks.

The cross-correlation functions of the neutron velocity spectra in the  ${}^7\text{Li}$  and  ${}^4\text{He}$  channels are shown in fig. 17. The velocity shift is  $v_s = -0.8$  cm/ns. The peaks No. 1. can be pileup peaks at 0 and 0.35 cm/ns, but the peaks in the  ${}^7\text{Li}$  channel at 1.10, 2.05, and 3.25 cm/ns can correspond to the 1.2–1.5, 2.4, and 3.1 cm/ns decay velocities.

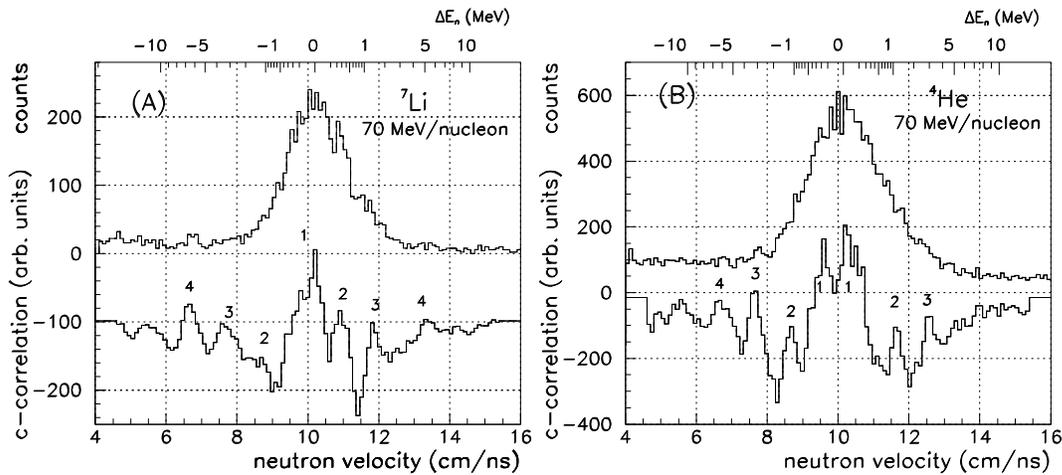


Figure 17: Neutron velocity spectra and the cross-correlation function of 70 MeV/nucleon  ${}^7\text{Li}+n$  and  ${}^4\text{He}+t+n$  reaction channels.

Similarly the 1.45, 2.40, and 3.30 cm/ns peaks of the  ${}^4\text{He}$  channel can be identified as the transitions with 1.3, 2.2, and 3.0 cm/ns decay velocities.

Summarizing please notice that the cross-correlation analysis gives valuable information about the behavior of a statistical mass, about its fluctuation. It was found that the structure of the velocity spectra of the neutrons from the prompt and delayed decay are identical, we can tell that in both mechanisms there are events from the same transitions. The two decay modes, the resonance and direct breakup must differ in the lifetime of the primary excited states. The delayed, resonance decay neutrons are low energy  $n_{II}$  neutrons but the prompt decay events have high decay energy primary neutrons too (fig. 15). In 40 MeV/nucleon the separation of the two mechanisms is worse than at 70 MeV/nucleon. The separated resonance decay events contain 34% prompt decayed events, therefore the resonance and direct breakup spectra are rather similar.

### 7.2. Fragment velocity of the prompt breakup events

In the Coulomb breakup the neutron and the fragment share the decay energy. The fragment gets the recoil velocity from the neutron emitted. The recoil velocity has a discrete value if the neutron is from a resonance decay. Additionally the fragment may get a continuous velocity component, the post-breakup acceleration if the decay happened in the Coulomb field of the target nucleus. The post-acceleration depends on the place of the decay, on the distance from the target nucleus. The velocity spectrum of the 40 MeV/nucleon  ${}^6\text{Li}$  fragments is shown in fig 18. The fragment velocity spectrum has a narrow central peak at  $v_0$  source velocity and some broader peak pairs fitted by four Gaussian functions. The S1 narrow peak is the resonance decay and the side peaks are from direct breakup events. The side peaks are asymmetric, cut by the detector acceptances and the magnetic field.

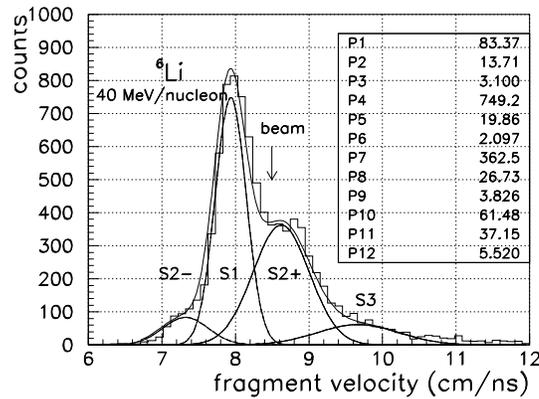


Figure 18: Fragment velocity spectrum of the  ${}^6\text{Li}$  channel at 40 MeV/nucleon energy.

The cross-correlation analysis of the fragment velocity spectra is shown in fig. 19. The fragment velocity spectra are compared to the neutron ones of the 70 MeV/nucleon  ${}^6\text{Li}+n$  resonance (A) and direct breakup (B) events. The fragment velocity spectra (b) are mirrored around the  $v_0$  source velocity and expanded to fit to the neutron ones (a). The expansion factor is  $R = 5.8$  and 4 of the resonance and direct breakup events, respectively. The agreement with the ratio of the mass numbers ( ${}^6\text{Li}$  and neutron), the momentum conservation verifies that the peaks are true ones, the neutron and the fragment are from one decay event, from a definite excited state of the  ${}^7\text{Li}$  in both resonance and direct breakup processes. In case of the direct breakup events the expansion factor is smaller. Probably the angular range is larger and the simplified estimation of the track length distorts the velocity scale. The comparison of the velocity spectra give similar result at 40 MeV/nucleon and for the  ${}^7\text{Li}$  and  ${}^4\text{He}$  fragments.

### 7.3. Fragment–neutron velocity correlation

The velocity correlation of a fragment–neutron pair can be investigated by the  $v_F$  vs  $v_n$  velocity surface plot. It verifies that the decay products originated from a common decay process and holds information about the time and place dependence of the decay. In fig. 20 there is shown the scatter plot of the 70 MeV/nucleon  ${}^6\text{Li}$  coincidence events. It is remarkable that there are fragments and neutrons faster than the beam. The velocity surface plot of the resonance decay events (A) is an isolated peak close to the beam velocity with  $\Delta v_F = \Delta v_n = -0.8$  cm/ns velocity deficit. The fig. 20(B) is the velocity surface of the  ${}^6\text{Li}$  direct breakup events. The plots are drawn in logarithmic scale to emphasize the structure of the velocity surface. The prompt decayed events have a texture, isles. The fluctuation suggests that the direct breakup events are also from discrete transitions, decayed inside the Coulomb field.

In order to understand the velocity surface plot one has to classify the decay modes. As a working hypotheses let us suppose, that the Coulomb dissociation is a two step process. The inverse population ratio suggests that in the approaching phase the projectile nucleus with valence neutron cannot decay, but suffers forced oscillation

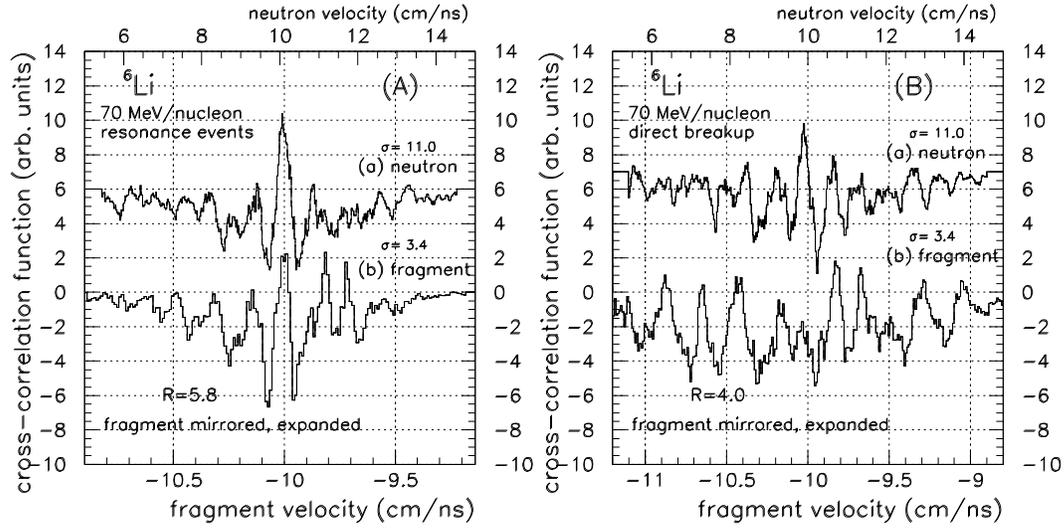


Figure 19: Comparison of the cross-correlation function of the  ${}^6\text{Li}$  fragment and the neutron velocities of the resonance (A) and direct breakup (B) events at 70 MeV/nucleon. The form function is a Gaussian shape function. The fragment spectra are mirrored and expanded to fit the neutron ones. The expansion factors are  $R = 5.8$  and  $4$ .

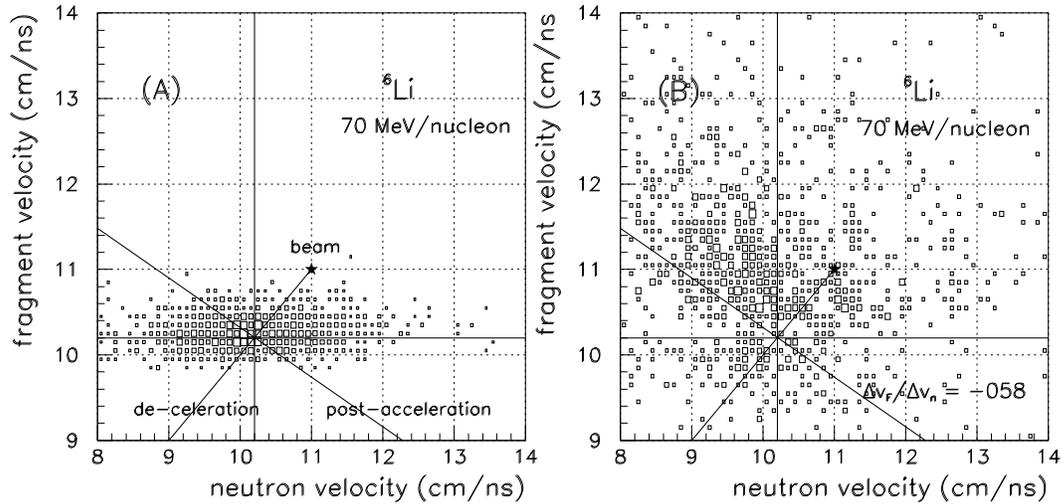


Figure 20: Velocity surface  $v_F$  vs  $v_n$  of 70 MeV/nucleon  ${}^6\text{Li}$  channel. (A) resonance and (B) direct breakup events (in logarithmic scale). The lines are the deceleration, post-acceleration, and  $v_0$  the excitation energy loss corrected beam velocity. The asterisks are the beam velocity.

and surpassing the closest approach point is trapped into a high energy primary excited state in the continuum: step I. The lifetime of the primary state can be large or small compared to the transit time of the projectile through the Coulomb field of the target nucleus. The primary excited state can decay prompt or delayed: groups P and D. The secondary excited state (step II.) may have also short or long lifetime. Four variations

can be DI&DII, DI&PII, PI&DII, and PI&PII. The DI&DII and the DI&PII groups are resonance decay events. The fragment is fully re-accelerated and gets the recoil velocity of the primary and secondary (final) decay. In the PI&DII group the primary excited state decays prompt in the Coulomb field of the target nucleus, the primary fragment escapes and decays in-flight. The detected fragment is post-accelerated with the  $Z/A$  of the primary fragment. It has the primary velocity deficit, the velocity excess got in the post-acceleration, and the recoil velocity of the primary and final decay. In the PI&PII group both decays happened in the Coulomb field simultaneously. The final fragment (of the secondary decay) is post-accelerated, got recoil velocity and has the velocity deficit.

The neutron velocity will be the momentary traveling velocity of the projectile, *i.e.* the source velocity, plus the decay velocity decreased by the fragment recoil. The events of the DI&any group give a spot on the deceleration line at  $\Delta v_F = \Delta v_n = v_x$  velocity deficit (fig. 20)(A). The PI&DII and the PI&PII events decay in the Coulomb field of the target nucleus. If the decay velocity is a discrete value, from the decay of a resonance state, the loci of the fragment–neutron velocities will be on a line parallel to the post-acceleration line. The large decay energy primary neutrons shift the post-acceleration line by the recoil corrected decay velocity  $v'_D = A_F/(A_F + 1) \cdot v_D$  to the right and down by the fragment recoil  $-v'_D/A_F$ . The above systematics results in a wedge shape velocity surface plot. The slope of the upper edge of the wedge gives the slope of the post-acceleration line, and the peak of the wedge gives the decay velocity (fig.20(B)).

The Coulomb energy slows down the projectile and deforms the orbit of the valence neutron. The velocity loss is regained, while the deformation energy is lost, frozen into excitation energy. Probably the selected impact parameter was less than 20 fm, the Coulomb potential of the  $^8\text{Li}$  is larger, for the velocity deficit itself is  $v_x = -0.8$  cm/ns which corresponds to 21 MeV excitation energy.

From the observations above one can conclude that the secondary decay inherits the lifetime of the primary excited state. The same final transitions may happen prompt or delayed. That results in the resonance decay and direct breakup processes. The decay mode is determined by the multipolarity of the orbit of the valence neutron. Probably the dominantly dipole excitations decay prompt and the multipole orbits live long. The decay modes are summarized in fig. 21.

Knowing the mass number of the fragment group, from the slope of the post-acceleration line one can get the  $Z$  charge of the fragment. The energy loss or gain of an ion in the Coulomb field at a distance  $r$  from the target nucleus is proportional with the  $Z/A$  ratio of the ion. If in the decay the  $Z/A$  ratio changes the fragment gets net velocity change. The measured quantities are the  $v_n$  neutron and  $v_F$  fragment velocities. The velocity change is the difference from the source velocity. The net velocity excess is the post-breakup acceleration. Supposing that in the moment of the decay the neutron velocity was equal with the projectile velocity, *i.e.*  $\Delta v_n(r) = \Delta v_p(r)$ , the neutrons preserve the velocity in the moment of the decay. Then the velocity excess, the post-

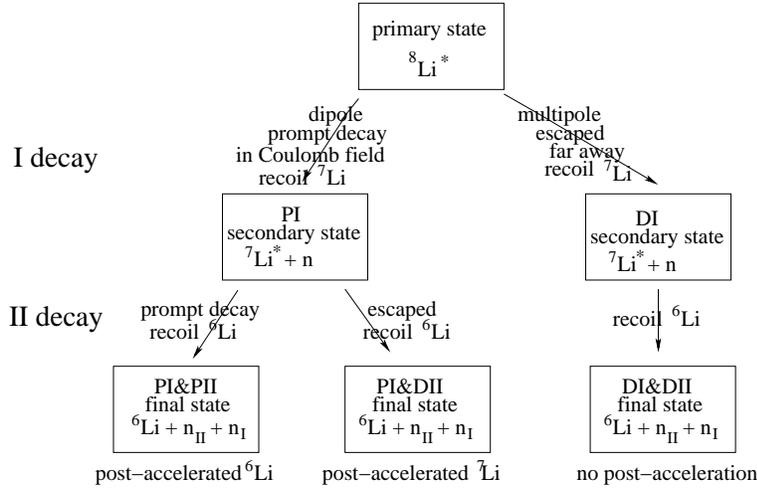


Figure 21: Flow diagram of the  ${}^6\text{Li}+2n$  Coulomb dissociation. The decay modes are: DI&DII double delayed, resonance decay, PI&PII double prompt decay, PI&DII primary prompt, secondary delayed, post-accelerated resonance decay.

breakup acceleration of the fragment is  $\Delta v_{pa} = \Delta v_F - \Delta v_p = \Delta v_F - \Delta v_n$ , and the relative velocity change of the fragment and the neutron is the slope of the post-breakup acceleration line  $m = \Delta v_{pa}/\Delta v_n = \Delta v_F/\Delta v_n - 1$ . On the other hand it was shown that the relative velocity increment can be given with the Z/A ratio of the projectile and the fragment:  $m = -\sqrt{\varepsilon} = -\sqrt{Z_F/Z_p \cdot A_p/A_F - 1}$  (Sec. 7).

**7.3.1.  ${}^6\text{Li}+2n$  channel** The velocity surface of the 40 MeV/nucleon  ${}^6\text{Li}+n$  coincidence events is shown in fig. 22. The plot (A) is a contour plot with single counts suppressed, to show the structure of the velocity surface of the  $n_{II}$  low velocity secondary neutrons. It has a wedge shape. The lines are the post-acceleration and the cross the beam velocity corrected by the excitation velocity loss.

In the velocity surface there are fragments and neutrons much faster than the beam. The projectile is slowed down in the approaching phase, and surpassing the closest approach point will be re-accelerated. The fragments of the prompt decay events get significant post-breakup acceleration. From the fig. 22(A) the slope of the upper edge of the wedge  $m = -0.58$  agrees with the post-acceleration of the  ${}^6\text{Li}$  ( $m = -\sqrt{8/6 - 1} = -0.58$ ). That means the  ${}^8\text{Li}$  projectile decayed somewhere in the Coulomb field and the second decay followed the primary decay in no time and the  ${}^6\text{Li}$  was accelerated (PI&PII). The plot (B) contains the high velocity primary neutrons too. The slope of the upper edge of the wedge is  $m = -0.38$ , which refers to the post acceleration of the intermediate  ${}^7\text{Li}^*$  fragment  $m = -\sqrt{8/7 - 1} = -0.38$ . The primary decay was prompt and the secondary one was delayed (PI&DII). The detected  ${}^6\text{Li}$  fragment was accelerated as  ${}^7\text{Li}$ . The upper edge of the wedge is a broad line formation, one can estimate the middle, the ridge of the line. In the plot (B) the peak of the wedge of the primary neutrons is about  $v'_D = 6-7$  cm/ns, which corresponds to

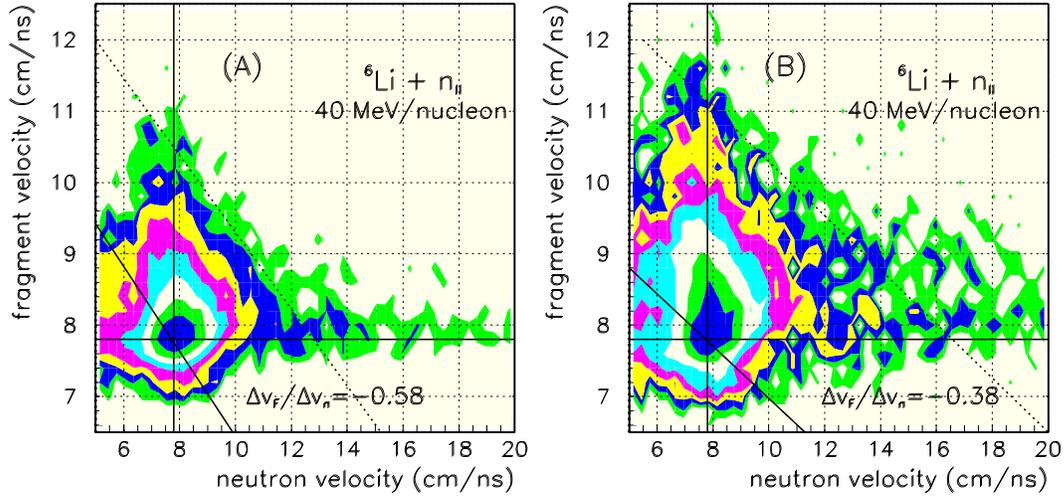


Figure 22: Contour plots of the velocity surface  $v_F$  vs  $v_n$  of 40 MeV/nucleon  ${}^6\text{Li}$  fragments in logarithmic scale. (A) secondary, low velocity neutrons (single counts suppressed), (B) primary neutrons. The lines are the excitation energy loss corrected beam velocity and the post-breakup acceleration lines. The dotted lines show the upper edge of the wedge.

$E_D = 22$  MeV decay energy.

The  ${}^7\text{Li}$  channel has no high velocity events above the beam velocity. Probably the projectile lost the excitation energy by  $\gamma$ -ray cascade, missed the channels opening and decayed from a low lying unbound resonance state of the  ${}^8\text{Li}$ . At both energies the  ${}^7\text{Li}$  is the end station of the relaxation of the  ${}^8\text{Li}$ . In fig. 23 the  ${}^4\text{He}$  velocity surface plots are compared at the two energies. The slope of the post-acceleration lines is  $-0.58$ . It is equal with  $\Delta v_F/\Delta v_n = -\sqrt{2/4 \cdot 8/3 - 1} = -0.58$ , the post-acceleration of the  ${}^4\text{He}$ .

The velocity surface analysis supports the identification of the  ${}^{6,7}\text{Li}$  and  ${}^4\text{He}$  fragments. The  ${}^2\text{H}$  and  ${}^6\text{He}$  channels are discussed in detail for they serve also valuable arguments for the particle identification and the reaction mechanism.

**7.3.2.  ${}^2\text{H}+{}^5\text{He}+n$  channel** The  ${}^2\text{H}$ -n coincidence events are the direct witnesses of the primary high excitation of the projectile. The threshold of the reaction is 11.65 MeV. The neutron velocity spectrum of the  ${}^2\text{H}$  channel is shown in fig. 24. The spectrum is unfolded by two Gaussian functions on an exponential background. The velocity increment of the high energy neutrons is about  $6.2 \pm 4$  cm/ns, which corresponds to 20.5 MeV decay energy.

The velocity surface of the  ${}^2\text{H}$ -n coincidence events is shown in fig. 25. The slope of the upper edge is  $m = -0.38$ . This support that the reaction is a two step decay:  ${}^8\text{Li} \rightarrow {}^7\text{Li} + n_I \rightarrow {}^5\text{He} + {}^2\text{H} + n_I$ , and the  ${}^7\text{Li}$  intermediate fragment is accelerated:  $\Delta v_F/\Delta v_n = -\sqrt{8/7 - 1} = -0.38$ . The fragment velocity excess goes up to 6 cm/ns. Probably the  ${}^2\text{H}$  channel is PI&DII type prompt decay, close to the closest approach point. The measured velocity excess of the  ${}^2\text{H}$  is the sum of the post-acceleration of the

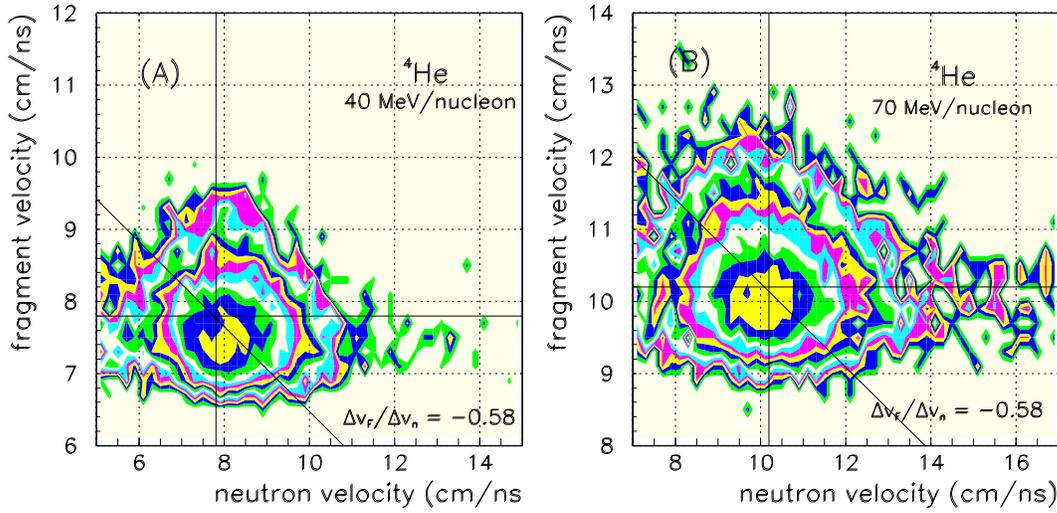


Figure 23: Velocity surface plots  $v_F$  vs  $v_n$  of  ${}^4\text{He}+t+n$  channel (A) 40 and (B) at 70 MeV/nucleon.

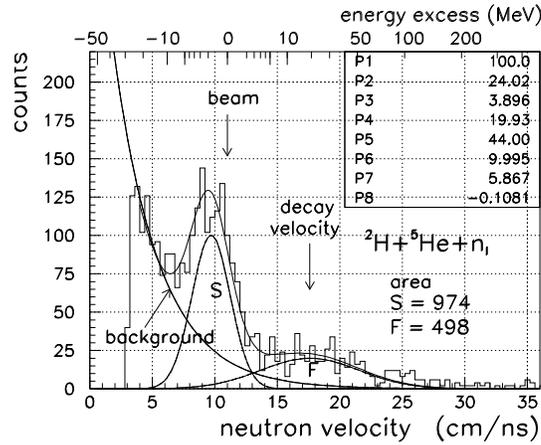


Figure 24: Neutron velocity spectrum of the  ${}^2\text{H}+{}^5\text{He}+n_I$  reaction channel at 70 MeV/nucleon.

${}^7\text{Li}$  primary fragment and the recoil velocity in the secondary  ${}^7\text{Li}\rightarrow{}^5\text{He}+{}^2\text{H}$  decay.

**7.3.3.  ${}^6\text{He}$  channel** The large yield of the  ${}^6\text{He}$  channel is a strong argument of the excitation into the giant resonance region. The threshold energy is 9.78 and 13.70 MeV. The  ${}^6\text{He}$  channel is the most intensive reaction channel at 40 MeV/nucleon, admitting that those are over represented accidental coincidences.

The velocity spectrum of the  ${}^6\text{He}$  (fig. 26) is an asymmetric peak. It is unfolded by 4 Gaussian functions. There is a narrow peak S1 at 8.8 cm/n with FWHM=0.35 cm/ns. It refers to a long lived resonance decay, although it is strongly cut by the CRDC telescope. The broader high energy tail D (the sum of 2 Gaussian functions) belongs to the post-accelerated, prompt decay in the Coulomb field of the target nucleus. And there is a small side peak S2 at about 7.8 cm/ns.

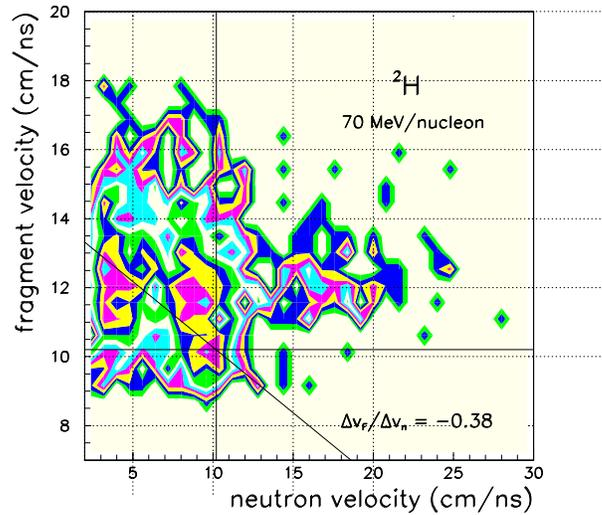


Figure 25: Velocity surface of  ${}^2\text{H}+{}^5\text{He}+n_I$  reaction channel at 70 MeV/nucleon.

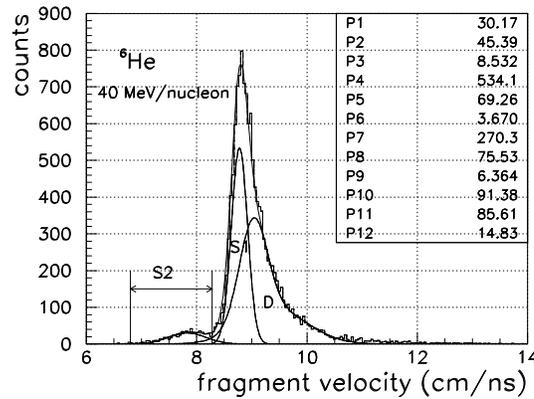


Figure 26:  ${}^6\text{He}$  velocity spectrum at 40 MeV/nucleon. The components are Gaussian fit results: S1 resonance decay, D direct breakup. (Fit parameters in 0.03 cm/ns units.) The S2 side peak is the  ${}^7\text{Li} \rightarrow \beta + {}^7\text{He} \rightarrow {}^6\text{He} + n$  reaction.

The neutron velocity spectrum in coincidence with the  ${}^6\text{He}$  fragments is an exponential decreasing one with a small bump at 8.1 cm/ns (fig. 27(a)). The exponential spectrum is an accidental coincidence spectrum because of the missing MoNA fast clear. The  ${}^6\text{He}$  has no neutron partner, probably it is from the  ${}^8\text{Li} \rightarrow {}^6\text{He} + d$  reaction channel. The small bump of the neutron velocity spectrum is in coincidence with the S2 side peak of the  ${}^6\text{He}$  velocity spectrum.

The MoNA bar frequency spectrum verifies that the neutrons are accidental ones (fig. 28(a)). The bar distribution shows a decreasing 16-th periodic structure, but the peaks are flat with a sharp peak in the lowest bars ( $16^{\text{th}}$ ,  $32^{\text{nd}}$ , *e.t.c*) scattered in from the floor and from the wall behind the detector. In the  ${}^6\text{He}$ -neutron coincidences the neutrons belong to a foreign fragment, to an other reaction in the time interval of the coincidence gate.

The cyclotron period was 45.82 ns (21.8259 MHz). The TDC range was 320 ns,

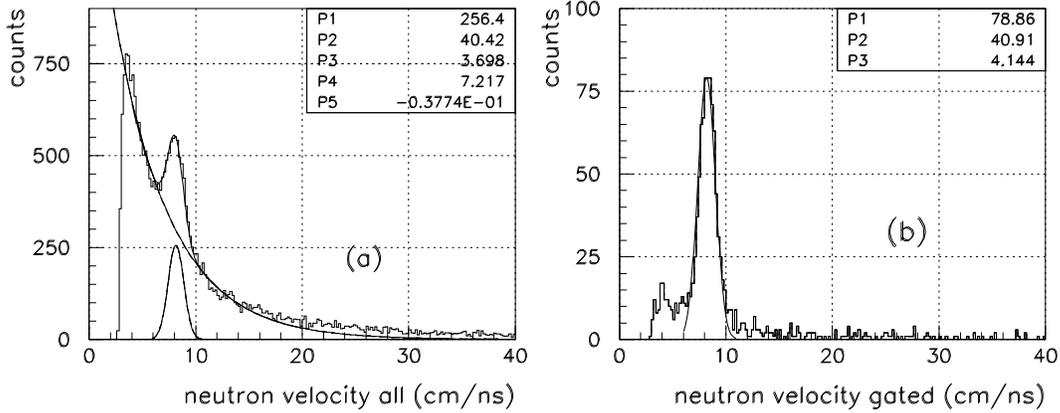


Figure 27: MoNA velocity spectra. (a) in coincidence with  ${}^6\text{He}$ , (b) neutron velocity spectrum cut by  ${}^7\text{He}$  gate (S2 in fig. 26). Fit parameters in 0.2 cm units.

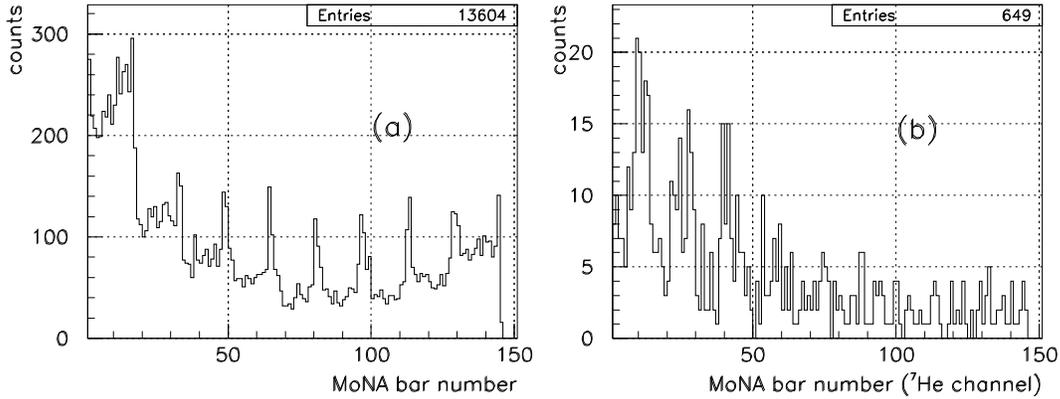


Figure 28: MoNA bar frequency in coincidence with  ${}^6\text{He}$  fragments at 40 MeV/nucleon. (a) all coincidence events, (b) gated by the S2 condition.

about 7 periods. The coincidence gate covered 3 cyclotron periods. The beam intensity was 150000/s, the average ion rate is 6.6 ion/ $\mu\text{s}$ , which gives 144 cycle/ion frequency. So at the beam intensity the cycles generally were empty, even probably there were a few percent spills with multiple ions in it. Supposedly the extraction from the ion source determines the beam structure. Really every event is fragment–MoNA coincidence event and the true coincident neutrons can be identified with valid TOF value, while the accidental neutrons generally went to overflow. The bar multiplicity of the true coincidence neutrons is 1–3 (fig. 2(b)).

The small bump at 7.8 cm/ns in the  ${}^6\text{He}$  velocity spectrum (fig. 26) belongs to true fragment–neutron coincidences. The neutron velocity spectrum gated by the  ${}^6\text{He}$  fragments signed by S2 is shown in fig. 27(b). It is a narrow neutron peak of FWHM=1 cm/ns. They are neutrons from the target in the center of the walls (fig. 28(b)). The MoNA hits can be neutrons — at these energies — from the reaction  ${}^8\text{Li}^* \rightarrow {}^7\text{Li} + n_I \rightarrow {}^7\text{He} + \beta^+ + n_I \rightarrow {}^6\text{He} + n_{II} + \beta^+ + n_I$ . The decay energy of the  ${}^7\text{He} \rightarrow {}^6\text{He} + n_{II}$  reaction is  $E_D = 0.44$  MeV. This decay channel is added to the decay

scheme of the  ${}^8\text{Li}$  shown in fig. 11. The  ${}^6\text{He}+d$  channel and the  ${}^6\text{He}+n$  channel both are resonance decay events with narrow fragment velocity spectrum.

The  $v_F$  vs  $v_n$  velocity surface is shown in fig. 29 of the  ${}^6\text{He}$  ions. The  ${}^6\text{He}$  velocity of the accidental coincidence events have a peak at 8.8 cm/ns, while the true coincident  ${}^6\text{He}$ -s are at  $v_0 = 7.8$  cm/ns. The velocity spectrum of the  ${}^6\text{He}$  of the deuteron channel is shifted up because of the recoil of the  ${}^6\text{He}$  by the 1.04 MeV deuteron. Further the acceptance of the FPD selects the fragments recoiled into the forward direction. The velocity surface plot verifies the fragment identification and the presence of the very intensive  ${}^6\text{He}$  fragments supports the leakage decay model of the Coulomb disintegration.

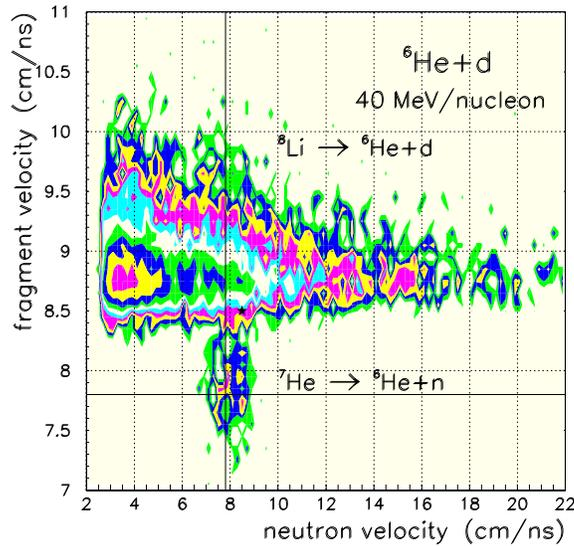


Figure 29: Velocity surface of the  ${}^6\text{He}+\text{MoNA}$  coincidences.

## 8. Leakage model of the decay and localized valence neutron model

Accepting the fragment identification, the high threshold and the inverse population ratio of the  ${}^7\text{Li}+n$ ,  ${}^6\text{Li}+2n$ ,  ${}^4\text{He}+t+n$ ,  ${}^6\text{He}+2n+\beta^+$ ,  ${}^6\text{He}+d$ , and  ${}^2\text{H}+n+{}^5\text{He}$  reaction channels, the equal velocity deficit, the identical structure of the velocity spectra of the prompt and delayed reaction products suggest that the Coulomb dissociation of a neutron rich light nucleus is a two step process. In the approaching phase the projectile is braked down by the Coulomb field of the target nucleus, and the orbit of the valence neutron is strongly deformed. The valence neutron gets forced oscillation. In the increasing Coulomb field the  ${}^8\text{Li}$  is not in its eigenstate and cannot decay. Similarly to the instantaneous model [11]. Passing the turning point, released, the ion will be trapped into a highly excited state which fits to the oscillation mode. The excited projectile traveling further will be re-accelerated and decays with the lifetime of the resonance state, emits a neutron or  $\gamma$ -rays. The dominantly single-particle, dipole excited states decay prompt, in the Coulomb field of the target nucleus, while the multipole excited states live long until the energy is concentrated to the valence neutron

and decay departing, in flight emitting a mono-energetic neutron. The above reaction mechanism can be called the *leakage model of the decay*. The highly excited primary states decay by high energy neutron emission or are degraded by  $\gamma$ -ray cascade. The rest of the beam will feed the lower energy channels. This results in the *inverse population ratio*, and that the share of the simplest  ${}^8\text{Li}^* \rightarrow {}^7\text{Li} + n$  channel is only 14 and 16% at 40 and 70 MeV/nucleon.

The collision of intermediate and high energy projectile is a sudden process. The orbital period of the valence nucleon is larger than the transit time of the projectile through the Coulomb field of the target nucleus. The interaction radius of the  ${}^8\text{Li}$  is  $r = 2.36 \pm 0.02$  fm [22]. Supposing that the mean radius does not change the  $E_x = 18$  MeV excitation energy corresponds to the frequency increment of the orbital motion.

$$E_x = \hbar\omega, \quad \nu = 4.47 \cdot 10^{21} \text{ s}^{-1}, \quad \text{and} \quad \Delta v_n = 6.6 \text{ cm/ns}$$

in agreement with the measured velocity increment (peak F in fig. 24). It can be supposed that during the impact the valence neutron stays in the forward or backward hemisphere of the projectile. According to the *localized valence neutron* assumption in the forward hemisphere the projectile gets a prolate deformation, dominantly dipole and single-particle excitation, and in the backward hemisphere oblate deformation, multipole and collective excitation. Basically two kinds of primary states can be excited corresponding to the position of the valence neutron during the impact: a short and a long living excited state according to the dipole or multipole deformation. The different reaction channels open through one of the primary excited states. The secondary breakup generally inherits the lifetime of the primary excited state. Therefore the fragments have a delayed narrow resonance like group in the velocity spectrum and a prompt broader one extended by the post-breakup acceleration. The multipolarity of the primary excited state is determined by the multipolarity of the orbit.

According to the Heisenberg Uncertainty Principle the momentum uncertainty of the localized neutron ( $\Delta x = 2.4$  fm) is  $\Delta p = 84$  MeV/c. The experiment could be close to this limit for at 40 MeV/nucleon the separation of the two mechanisms is less sharp than at 70 MeV/nucleon. At the impact parameter scale the wedge shape of the velocity surface, the post-acceleration gives information about the position or the time of the decay in the Coulomb field of the target nucleus. The post-acceleration is a clock of the reaction [12].

## 9. Summary

The paper presents the analysis of experimental data from Coulomb dissociation of  ${}^8\text{Li}$  on Pb target at 40 and 70 MeV/nucleon energy. The  ${}^6,7\text{Li}$ ,  ${}^4,6\text{He}$ , and  ${}^2\text{H}$  fragments are separated.

The two mechanisms of the Coulomb dissociation, the soft dipole resonance and the direct breakup are demonstrated. The resonance decay, discrete low decay energy neutrons are identified in the  ${}^8\text{Li} \rightarrow {}^6\text{Li} + 2n$  dissociation and the post-breakup

acceleration of the prompt, direct breakup fragments is verified. It was found that the structure of the neutron velocity spectra of the two reaction mechanisms is identical. It has to be supposed that the Coulomb dissociation is a two step process. The primary excited states may have short or long lifetime, so the neutrons of the secondary decay, from the same transitions, can appear prompt or delayed related to the projectile. The secondary decay inherits the lifetime of the primary decay. The decay, primary or secondary, in the Coulomb field of the target nucleus results in the post-breakup acceleration of the fragment.

The threshold of the reaction channels is high, more than 10 MeV. The velocity loss of the resonance decay products corresponds to about 21 MeV excitation energy at the given magnetic field and impact parameter set, at both energies and for every reaction channels. Probably the primary excited states are common for the channels. The secondary excited states are fed from up downwards by the rest of the beam. It is called *leakage decay model* of the Coulomb dissociation. That results in the *inverse population ratio* of the reaction channels, *i.e.* the higher the energy of the secondary excited state, the larger is the probability of the decay through that channel.

The intermediate and high energy collisions are sudden reactions, the orbital period of the valence neutron is larger than the transit time of the projectile through the Coulomb field of the target nucleus. The sudden reaction allows the *localized valence neutron model*, that the valence neutron stays in the forward or backward hemisphere of the projectile during the impact. Corresponding to the position of the valence neutron the deformation of the forced oscillation will be prolate, dominantly dipole or oblate, multipole oscillation, single-particle or collective excitation. which determines the lifetime of the excited state.

The conclusion of the paper is: the data give experimental evidence that a quantum system under the effect of an increasing long range external force gets forced oscillation and cannot fall into an eigenstate of its subsystem, but the force pushes it through several states up to the giant resonance region. In the Pb+core+valence neutron+electromagnetic field quantum system the orbit of the valence neutron deforms quasi continuously and passing the closest approach point, released the nucleus is trapped into a highly excited state which fits to the quantum numbers of the oscillation. The highly excited state decays with own lifetime delayed or prompt giving the soft dipole resonance and the so called 'direct breakup' decay mechanisms of the Coulomb dissociation. The direct breakup is really also resonance decay of the low lying unbound resonance state but prompt even in the strong Coulomb field.

## Acknowledgments

The author is indebted to Vladimir Zelevinsky for his stimulation and valuable discussions, to Aaron Galonsky for his substantial remarks and advices, and to Rudolf Izsák for his cooperation and technical help. The author is grateful to the MoNA collaboration that made available the experimental data. The participants of the MoNA collaboration

are: M. Csanád<sup>1</sup>, F. Deák<sup>1</sup>, Á. Horváth<sup>1</sup>, R. Izsák<sup>1</sup>, Á. Kiss<sup>1</sup>, G. I. Veres<sup>1</sup>, Z. Seres<sup>2</sup>, T. Baumann<sup>3</sup>, D. Bazin<sup>3</sup>, N. Frank<sup>3</sup>, A. Gade<sup>3</sup>, D. Galaviz<sup>3</sup>, A. Galonsky<sup>3</sup>, A. Schiller<sup>3</sup>, M. Toennessen<sup>3</sup>, P. DeYoung<sup>4</sup>, W. A. Peters<sup>5</sup>, K. Ieki<sup>6</sup>, R. Sugo<sup>6</sup>, T. Fukuchi<sup>7</sup>, Zs. Fülöp<sup>8</sup>, C. A. Bertulani<sup>9</sup>, H. Schelin<sup>10</sup>, N. Carlin<sup>11</sup>, and C. Bordeanu<sup>12</sup>. The support of the Hungarian OTKA grant No. T049837 and the National Science Foundation under Nos. Phy01-10253, PHY03-54920, and PHY04-56463 are gratefully acknowledged.

<sup>1</sup>*Department of Atomic Physics, Eötvös Loránd University, H-1117 Budapest, Hungary*

<sup>2</sup>*Institute for Particle and Nuclear Physics, Wigner Research Centre for Physics, H-1525 Budapest, Hungary*

<sup>3</sup>*National Superconducting Cyclotron Laboratory, Michigan State University, East Lansing, Michigan 48824, USA*

<sup>4</sup>*Department of Physics and Engineering, Hope College, Holland, Michigan 49423, USA*

<sup>5</sup>*University of Tennessee, ORNL, Physics Division, Oak Ridge, TN 37831, USA*

<sup>6</sup>*Department of Physics, Rikkyo University, 3 Nishi-Ikebukuro, Toshima, Tokyo 171, Japan*

<sup>7</sup>*RIKEN Center for Life Science Technologies, Kobe, Hyogo 650-0047, Japan*

<sup>8</sup>*ATOMKI Institute for Nuclear Research, H-4001 Debrecen, Hungary*

<sup>9</sup>*Department of Physics and Astronomy, Texas A&M University–Commerce, Commerce, Texas 75429, USA*

<sup>10</sup>*Federal University of Technology–Parana, 80230-901 Curitiba, Paraná, Brazil*

<sup>11</sup>*Instituto de Física, Universidade de São Paulo, 05315-970 São Paulo, Brazil*

<sup>12</sup>*National Institute for Physics and Nuclear Engineering - Horia Hulubei, Măgurele-Bucharest, Romania, 07125*

## References

- [1] Á. Horváth *et al.*, *Eur. Phys. J. A* **27** s01, 217–220 (2006).
- [2] R. Izsák *et al.*, *Phys. Rev. C* **88**, 065808 (2013).
- [3] P. G. Hansen and B. Jonson, *Europhys. Lett.* **4** (4), 409-414 (1987).
- [4] A. Galonsky *et al.*, *Nucl. Phys. A* **599**, 353c-366c (1996).
- [5] K. Ieki *et al.*, *Phys. Rev. Lett.* **70**, 730-733 (1993).
- [6] H. Sagawa, N. Van Giai, N. Takigawa, M. Ishihara, and K. Yazaki, *Z. Phys. A* **351**, 385-389 (1995).
- [7] R. Anne *et al.*, *Nucl. Phys. A* **575**, 125-154 (1994).
- [8] J. E. Bush *et al.*, *Phys. Rev. Lett.* **81**, 1, 61 (1998).
- [9] K. Riisager *et al.*, *Nucl. Phys. A* **540**, 365 (1992).
- [10] D. Sacket *et al.*, *Phys. Rev. C* **48**, 118 (1993).
- [11] G. Baur, C.A. Bertulani, and D.M. Kalassa, *Nucl. Phys. A* **550**, 127-530 (1992)
- [12] C. A. Bertulani and G. Baur, *Nucl. Phys. A* **458**, 725-744 (1986).
- [13] G. F. Bertsch and C. A. Bertulani, *Nucl. Phys. A* **556**, 136-146 (1992).
- [14] T. Kido, K. Yabana, and Y. Suzuki, *Phys. Rev. C* **53**, 5, 2296-2303 (1996).
- [15] C. A. Bertulani, *Brasilian Journal of Physics*, vol. **26**, no. **3**. September, 1996
- [16] D. J. Morrissey *et al.*, *Phys. Rev. C* **32**, 877 (1985)
- [17] R. Izsák, Ph.D. thesis, ELTE University, Budapest, 2014.
- [18] T. Baumann *et al.*, *Nucl. Instrum. Methods, A* **543**, 517 (2005).

- [19] M. Bird *et al.*, and A. F. Zeller, *Applied Superconductivity, IEEE Transactions on* **15**, 1225 (2005).
- [20] J. Yurkon *et al.*, *Nucl. Instrum. Methods in Physics Research Section A: Accelerators, Spectrometers, Detectors, and Associated Equipment* **422**, 291 (1999).
- [21] F. Ajzenbeg-Selov, *Nucl Phys.* **A320**, 1 (1979).
- [22] F. Ajzenbeg-Selov, *Nucl Phys.* **A490**, 1 (1988).
- [23] A.L. Conneley and W.W. Black, *Nucl. Instr. and Meth.* **82** (1970) 141–148.